Size-frequency distributions of rocks on the northern plains of Mars with special reference to Phoenix landing surfaces

M. P. Golombek,[1] A. Huertas,[1] J. Marlow,[2,3] B. McGrane,[4] C. Klein,[5] M. Martinez,[6] R. E. Arvidson,[2] T. Heet,[2] L. Barry,[2] K. Seelos,[7] D. Adams,[1] W. Li,[8] J. R. Matijevic,[1] T. Parker,[1] H. G. Sizemore,[9] M. Mellon,[9] A. S. McEwen,[10] L. K. Tamppari,[1] and Y. Cheng[1]

[1] The size-frequency distributions of rocks >1.5 m diameter fully resolvable in High Resolution Imaging Science Experiment (HiRISE) images of the northern plains follow exponential models developed from lander measurements of smaller rocks and are continuous with rock distributions measured at the landing sites. Dark pixels at the resolution limit of Mars Orbiter Camera thought to be boulders are shown to be mostly dark shadows of clustered smaller rocks in HiRISE images. An automated rock detector algorithm that fits ellipses to shadows and cylinders to the rocks, accurately measured (within 1−2 pixels) rock diameter and height (by comparison to spacecraft of known size) of ∼10 million rocks over >1500 km^2 of the northern plains. Rock distributions in these counts parallel models for cumulative fractional area covered by 30−90% rocks in dense rock fields around craters, 10−30% rock coverage in less dense rock fields, and 0−10% rock coverage in background terrain away from craters. Above ∼1.5 m diameter, HiRISE resolves the same population of rocks seen in lander images, and thus size-frequency distributions can be extrapolated along model curves to estimate the number of rocks at smaller diameters. Extrapolating sparse rock distributions in the Phoenix landing ellipse indicate <1% chance of encountering a potentially hazardous rock during landing or that could impede the opening of the solar arrays. Extrapolations further suggest rocks large enough to depress the ground ice table and small enough to be picked up or pushed by the robotic arm should be present within reach for study after landing.

1. Introduction

[2] The size-frequency distribution of rocks on Mars is important for understanding the geologic and geomorphic history of a surface [*Garvin et al.*, 1981; *Craddock et al.*, 2000; *Yingst et al.*, 2007; *Grant et al.*, 2006], for quantifying the hazards for landing spacecraft, and evaluating the trafficability for roving [*Golombek and Rapp*, 1997; *Golombek et al.*, 2003]. The Phoenix lander will determine the chemical composition of soil overlying ice [*Smith et al.*, 2008] and rocks at the surface will produce variations in the dry layer thickness due to their higher thermal inertia [*Sizemore and Mellon*, 2006]. Rocks could thus produce gradients in moisture in the soil or even potential habitats that can be investigated with the robotic arm. In addition, pebbles can be picked up by the arm [*Bonitz et al.*, 2008] and examined by the imagers, thereby allowing investigations of rock texture, color and spectra. Because of its design, the Phoenix lander is sensitive to rocks on landing that can cause lander tilt or tip over with remaining horizontal velocity, that can impact the underside and damage the lander, and that can prevent complete opening

[1]Jet Propulsion Laboratory, California Institute of Technology, Pasadena, California, USA.
[2]Department of Earth and Planetary Sciences, Washington University at St. Louis, St. Louis, Missouri, USA.
[3]Now at Department of Earth Science and Engineering, Imperial College, London, UK.
[4]Department of Geology, Occidental College, Los Angeles, California, USA.
[5]Department of Astronomy, California Institute of Technology, Pasadena, California, USA.
[6]Department of Aeronautics and Astronautics, University of Washington, Seattle, Washington, USA.
[7]Applied Physics Laboratory, Johns Hopkins University, Laurel, Maryland, USA.
[8]Department of Computation and Neural Systems, California Institute of Technology, Pasadena, California, USA.
[9]Laboratory for Atmospheric and Space Physics, University of Colorado, Boulder, Colorado, USA.
[10]Lunar and Planetary Laboratory, University of Arizona, Tucson, Arizona, USA.
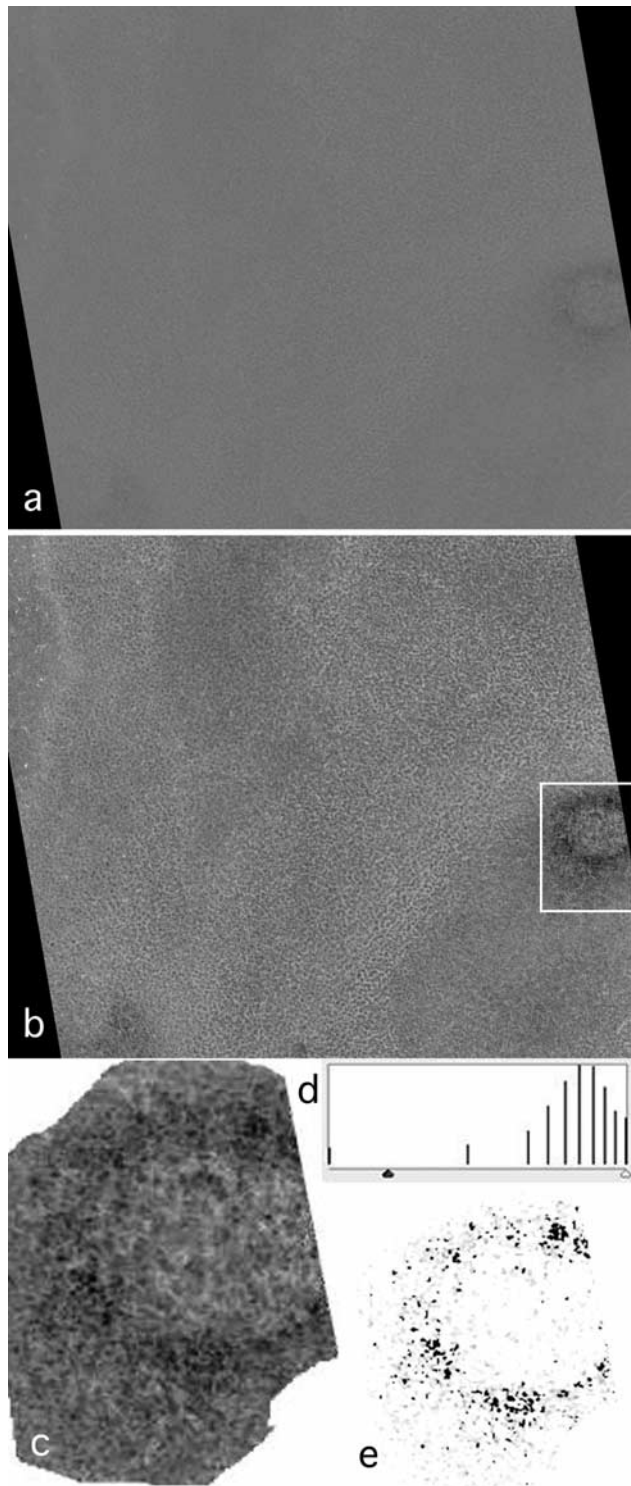
Figure 1. Derivation of the cumulative fractional area of boulders in MOC image. (a) A segment of an original MOC narrow angle image R20-00731 (with resolution of 3.39 m/pixel, solar azimuth 306.2°, solar elevation 41°). (b) The image is stretched to increase contrast and reveal areas of high boulder density. (c) Boulder field marked in Figure 1b is isolated. (d) The histogram of gray scale is viewed and stretched such that only pixels designated as boulders remain visible. (e) These remaining "boulder pixels" are then divided by total pixels to determine the cumulative fractional area covered by boulders.

of the solar arrays after landing (see *Arvidson et al.* [2008] for an overview of the Phoenix landing site selection process). Understanding the distribution of rocks at prospective landing sites from remotely sensed data is thus critical to mission success.

[3] Prior to Phoenix all landing site selection efforts have relied on thermal differencing techniques applied to Infrared Thermal Mapper (IRTM) [*Kieffer et al.*, 1977] data to estimate the cumulative fractional area covered by rocks greater than about 10 cm diameter [*Christensen*, 1986]. Prior to landing Mars Pathfinder, IRTM rock abundance
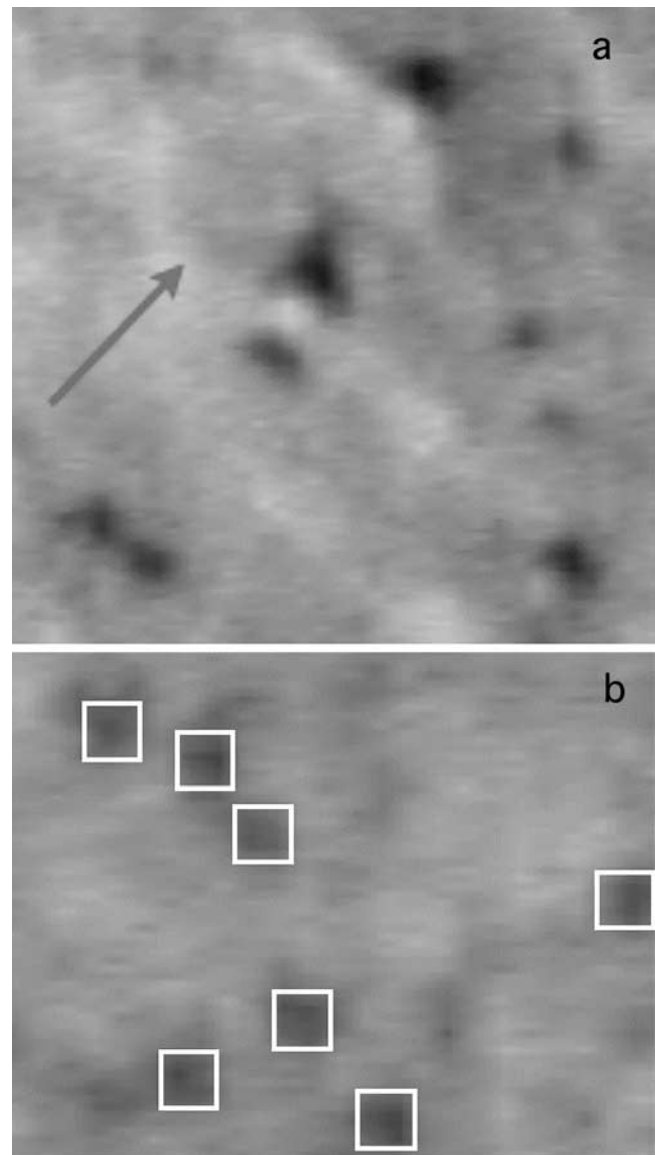

Figure 2. Boulders in cPROTO MOC image, S02-01184 with a resolution of 50 cm per pixel. (a) Boulders have bright sunlit sides and shadows that taper in the direction of sunlight (arrow) from the southwest (solar azimuth of 223.6°; solar elevation 28.3°). Shadows indicate the presence of raised features on the surface, interpreted as boulders. (b) Image shows that the average boulder resolvable in the cPROTO image corresponds roughly to the size of a standard single MOC narrow angle image pixel (shown by the white boxes, which are 3.5 m on a side).
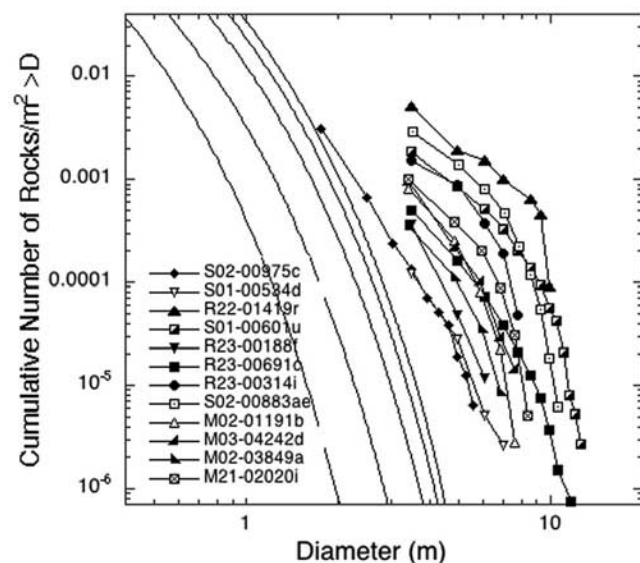
Figure 3. Graph of cumulative number of boulders larger than a given diameter per square meter versus boulder diameter for 12 representative boulder fields in MOC images. Lines to the left are cumulative number curves that correspond to exponential model cumulative fractional area distributions based on rocks measured in lander images for 5%, 10%, 20%, 30%, and 40% (from left to right) cumulative fractional area rock coverage. The size-frequency distributions of the selected fields show a similar steep decrease in number with increasing diameter comparable with the model distributions but are shifted to larger diameters. Cumulative fractional area (CFA) correlates well with cumulative number of boulders (CN) for regions with size-frequency count data in MOC images of prospective Phoenix landing regions (CFA = 16.6 CN with a correlation coefficient of 0.92 for 136 boulder fields). This indicates that cumulative fractional area can be used as a reliable proxy for the cumulative number for probability calculations [e.g., *Marlow et al.*, 2006].

data were combined with surface rock counts at the Viking Lander 1 and 2 (VL1, VL2) sites and rocky locations on Earth to develop a model of the cumulative fractional area covered by rocks of any size and larger versus diameter for the centimeter to 1 m size rocks observed at the landing sites [*Golombek and Rapp*, 1997]. The size-frequency distributions of rocks at the VL1 and 2 sites were fit with simple exponential curves of the form

$$F_k(D) = k \exp[-q(k)D], \qquad (1)$$

where $F_k(D)$ is the cumulative fractional area covered by rocks of diameter D or larger, k is the total area covered by all rocks, and an exponential q(k), which governs how abruptly the area covered by rocks decreases with increasing diameter [*Golombek and Rapp*, 1997]. These models were used by assuming that k is equal to the rock abundance determined by the IRTM thermal differencing and calculating the cumulative fractional area covered by rocks greater than any particular diameter of concern [*Golombek and Rapp*, 1997; *Golombek et al.*, 2003]. Even though the IRTM estimates are at a spatial resolution of 1 degree bins (~60 km) [*Christensen*, 1986], comparisons with rock counts at the surface at much smaller scales have been remarkably successful at all 5 landing sites [*Moore and Jakosky*, 1989; *Christensen and Moore*, 1992; *Golombek et al.*, 1999, 2005, 2008] in terms of the total area covered by rocks as well as the cumulative fractional area versus diameter distribution matching the exponential model for rocks >10 cm.

[4] *Golombek and Rapp* [1997] argued that the underlying cause for the exponential size-frequency distributions observed is fracture and fragmentation theory [e.g., *Rosin and Rammler*, 1933; *Gilvarry*, 1961; *Gilvarry and Bergstrom*, 1961], which predicts that ubiquitous flaws or joints will lead to exponentially fewer blocks with increasing size during weathering and transport [e.g., *Wohletz et al.*, 1989; *Brown and Wohletz*, 1995]. The corresponding cumulative number versus diameter distributions appear steeper and match model curves derived by numerical integration as there is no analytic method to go from the cumulative fractional area relationship to a cumulative number relationship (see discussion by *Golombek and Rapp* [1997] and *Golombek et al.* [2003]). These cumulative number model distributions can then be easily used to determine the probability of encountering a rock of any given size over some area for any total rock abundance, which was used for evaluation of the Mars Exploration Rover (MER) landing sites [*Golombek et al.*, 2003].

[5] The identification of boulders in high-resolution Mars Orbiter Camera (MOC) images at around 3 m/pixel did not help much in the evaluation of rock hazards because it was unclear how the distributions of boulders with diameters greater than ~5 m related to distributions of much smaller diameter rocks seen at the surface [*Golombek et al.*, 2003]. Further, even though higher spatial resolution thermal differencing estimates of rock abundance are now available from Thermal Emission Spectrometer (TES) [*Nowicki and Christensen*, 2007], none of these estimates extend poleward of 60° latitude due to icy and cold atmospheres, so this approach could not be used for Phoenix landing site selection and was recognized as a serious uncertainty early

Table 1. Statistics of Boulder Fields in MOC Images

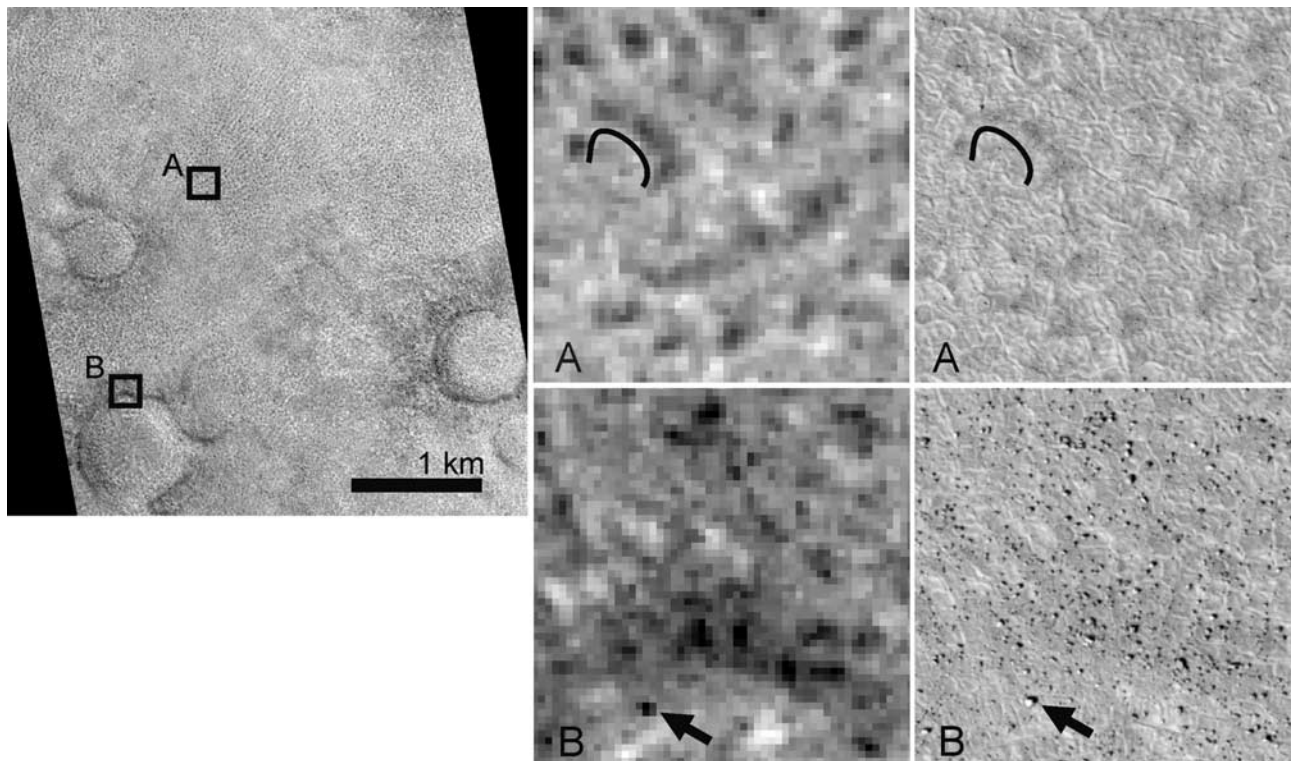| Region	Percent of Surveyed Area Covered by Boulder Fields	Percent of Boulder Field Area Occupied by Boulders	Percent of Surveyed Area Occupied by Boulders	Square Kilometers per Boulder Field	Number of MOC Images Surveyed	Number of Boulder Fields
A	2.1	1.0	0.02	32.1	54	69
B	7.4	1.6	0.12	4.8	191	1247
C	4.2	0.9	0.04	5.4	42	308
Total	5.6	1.5	0.08	6.0	287	1624

GOLOMBEK ET AL.: HIRISE ROCKS

Figure 4. Region B comparison of boulder appearances in MOC and HiRISE data. (left) MOC image R20-00082 (3.4 m/pixel; 41° solar elevation; 224° solar azimuth) covers a typical terrain consisting of patterned ground (box A) and degraded craters with dark rims (box B). (middle) Areas A and B are shown enlarged (right) along with corresponding HiRISE data from image TRA_00828_2495 (0.25 m/pixel; 36.4° solar elevation; 194° solar azimuth). In MOC subset A, patterned ground is revealed to be clusters of small rocks tens of centimeters in diameter. In MOC subset B, the crater rim is generally made up of larger boulders that are more scattered. However, both of these distributions create the same patchy albedo appearance in MOC data. Image subsets are 175 m wide, and illumination is from the lower left. Lines and arrows indicate equivalent features in each image.
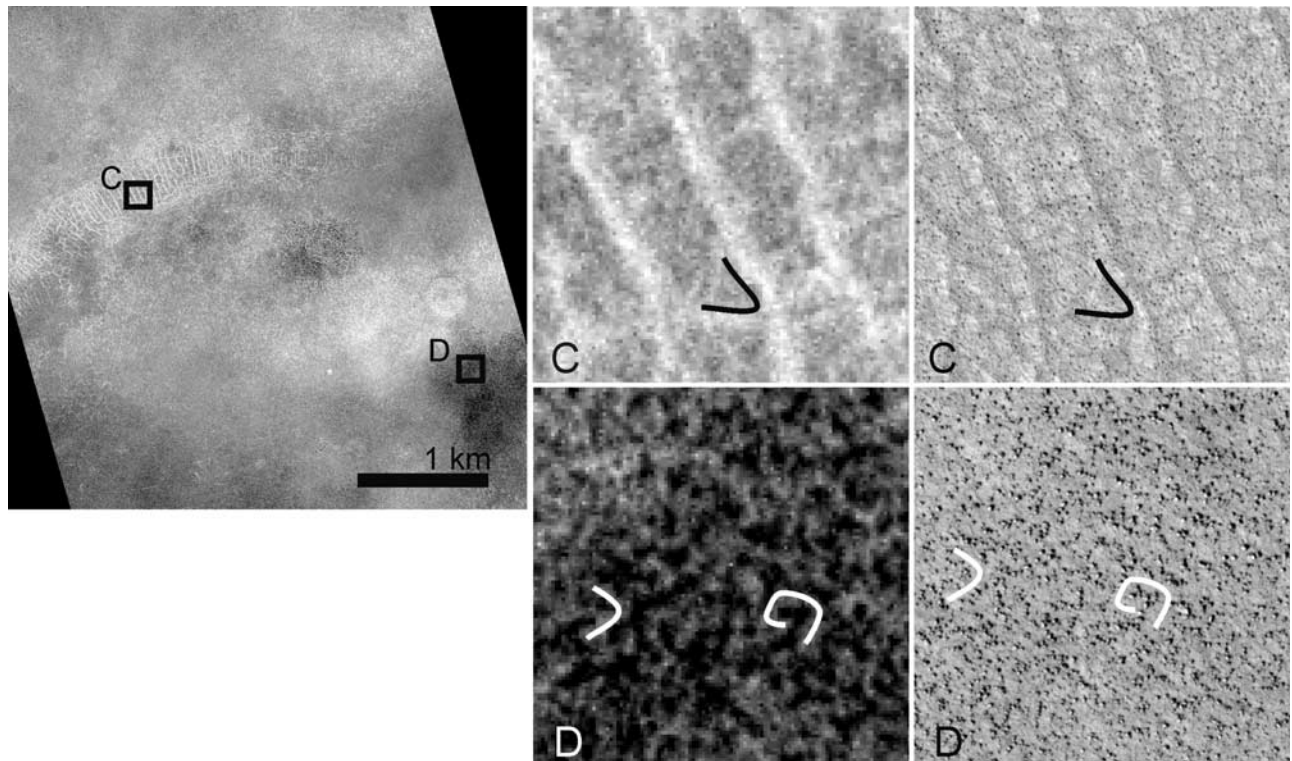
Figure 5. Region B comparison of boulder appearances in MOC and HiRISE data. (left) MOC image S16-01240 (1.7 m/pixel; 32° solar elevation; 211° solar azimuth) illustrates surfaces associated with multiple-kilometer polygons, including rectilinear trough polygons (C) and dark interior plains (D). The rectilinear polygons shown in area C (top center) exhibit moderate albedo variability in MOC data, with bright springtime frost outlining the polygon troughs. The corresponding HiRISE subset from image TRA_00841_2460 (0.25 m/pixel; 38° solar elevation; 190° solar azimuth) at the right shows small boulders distributed along the trough boundaries and within the interiors, making for a fairly uniform, moderate albedo appearance. The dark plains of the multiple-kilometer polygon (area D, lower middle and right) are similarly uniform, but in this case associated with a dense field of large boulders. Image subsets are 175 m wide, and illumination is from the lower left. Lines illustrate equivalent features.
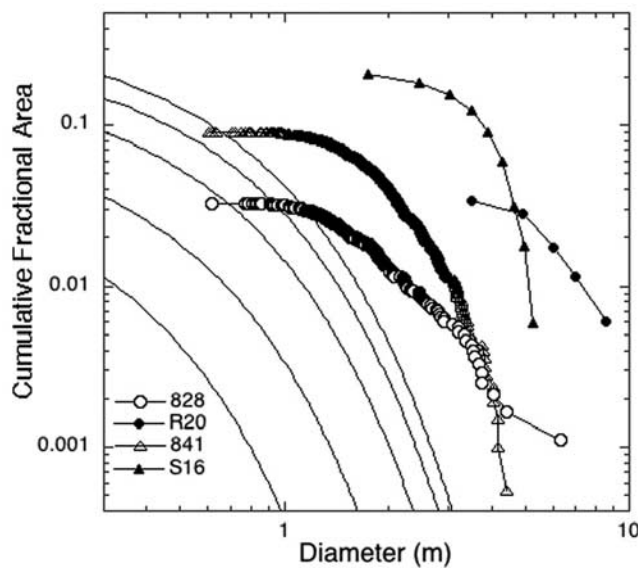
Figure 6. Cumulative fractional area versus diameter distribution of the same areas in MOC (solid symbols) and HiRISE images (open symbols) shown in Figures 4, area B (circles), and 5, area D (triangles). Also shown are exponential model distributions corresponding to (from left to right, respectively) 5%, 10%, 20%, 30%, and 40% cumulative fractional area covered by rocks.

on in the selection process [*Marlow et al.*, 2006; *Putzig et al.*, 2006, *Golombek et al.*, 2007]. These concerns turned into reality with the return of the first HiRISE (High Resolution Imaging Science Experiment) images of the northern plains of Mars, which showed prospective landing surfaces littered with large rocks that would be fatal to the Phoenix lander [*McEwen et al.*, 2007b; *Arvidson et al.*, 2008].

[6] In this paper, rocks clearly visible in HiRISE images [*McEwen et al.*, 2007a, 2007b] are counted and compared with distributions measured from the surface at the successful landing sites. First, the distributions of dark boulders in MOC images in prospective Phoenix landing site regions are described and quantified. Next, HiRISE images of the same features are described and the size frequency distributions are compared with those derived from MOC. A new method for automatically counting rocks [*Huertas et al.*, 2006] from their shadows in HiRISE images is described and tested, and rock counts are compared with those counted at the successful landing sites. These comparisons show for the first time that rocks identified from orbit are part of the same size-frequency distribution as those counted from the ground and provide a straightforward way to extrapolate the number of rocks to any size of concern. Finally we use these distributions to estimate the probability of encountering rocks during landing, when opening the solar arrays, and during robotic arm investigation of surface materials. Results indicate that areas with low rock abundance in HiRISE images likely have very few rocks large enough to cause difficulties during landing or opening of the solar arrays,

and there should be a multitude of small rocks in the robotic work space for investigation with the robotic arm after landing.

2. Boulders Identified in MOC Images

[7] Early in the site selection process before Mars Reconnaissance Orbiter was at Mars, the landing site selection team evaluated potential hazards in three areas under consideration for landing Phoenix [*Arvidson et al.*, 2008]. MOC images were acquired within target $65° – 72°N$ latitude areas A ($250° – 270°E$), B ($120° – 140°E$), and C ($65° – 85°E$) initially identified for landing Phoenix. Anomalously dark pixels in MOC narrow angle images (~ 3 m/pixel) of the northern plains had been identified as boulders by *Malin and Edgett* [2001]. They are found in low-albedo clusters typically located around degraded or pedestal craters in the northern plains, which have been interpreted as surface lag resulting from eolian deflation of crater ejecta [e.g., *McCauley*, 1973; *Arvidson et al.*, 1976, 1979; *Greeley et al.*, 2001]. Other areas without obvious relationship to craters with a prevalence of dark pixels at similar color contrast are also likely boulder fields (Figure 1). Further justification for the identification of the dark pixels as boulders in MOC images comes from analysis of a MOC planetary-motion-compensated Pitch and Roll Targeted Observation (cPROTO) image [*Malin and Edgett*, 2001] in which the signal-to-noise ratio is improved and the down track smear is reduced, enabling the 1.5 m instantaneous field of view (IFOV) to limit the resolution; images are resampled on the ground to 50 cm/pixel. Shadows taper in accordance with solar azimuth (implying the presence of topographic highs) and dark patches (the shadows) are equivalent in area to a single pixel in a normal MOC image (Figure 2). As a result, at the highest resolution possible from MOC, the dark pixels in the northern plains appear similar to obvious large boulders in the equatorial region that have clear bright, sunlit and dark, shadow sides [*Golombek et al.*, 2003].

[8] To determine the area covered by dark boulders in MOC images, gray scale levels were adjusted manually to optimize visibility of high boulder density regions, which were then outlined. Within each outlined boulder field, image contrast was further stretched and the number of dark pixels designated as boulders was divided by the total number of pixels to derive the cumulative fractional area, or percentage of the surface that consists of boulders (Figure 1). The size-frequency of boulders was counted in a subset of boulder fields with a range of total area covered by boulders (equivalent to the cumulative fractional area). Each blob or group of dark pixels was assumed to be a single boulder, whose area was represented by the area of dark pixels and were tabulated as 1 pixel, 2 pixels, 3 pixels and so on. The area of each pixel was multiplied by the number of dark pixels and assumed to be the area of the boulder, from which a diameter was calculated. This allowed determination of the cumulative fractional area covered by rocks of a given diameter and larger and the cumulative number of boulders larger than a given diameter per meter squared versus diameter. The latter plot is shown in Figure 3, which shows that the size-frequency distribu-
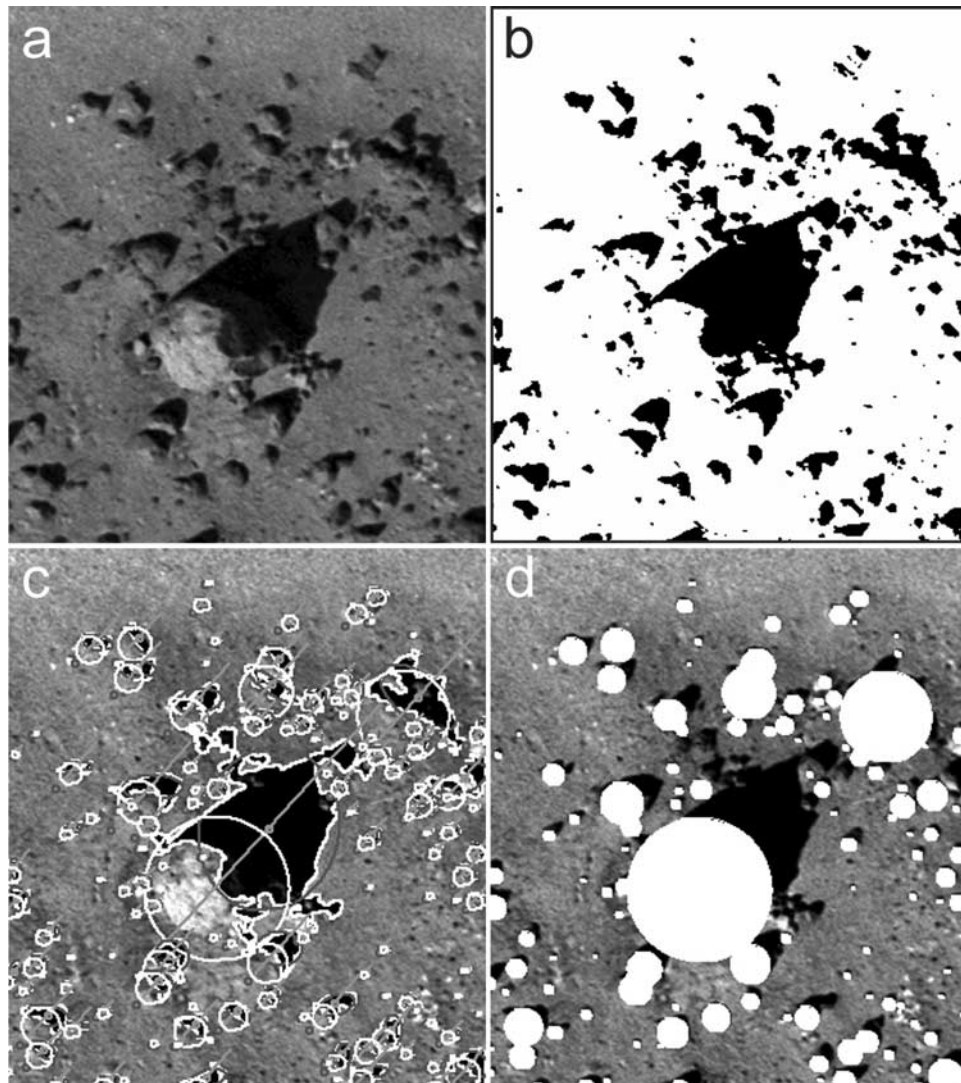
Figure 7. Shadow-based rock detection in 320 × 360 pixel subimage at 0.037 m/pixel image that spans a 12 m × 13.5 m area Mars Hill in Death Valley, California. (a) Image shows rocky surface with long shadows. Large boulder in the center is 3 m in diameter. (b) Shadow segmentation classifies the image into shadow and nonshadow areas. (c) White lines outline the shadows, which are fit with ellipses. (d) Cylinders are fit to the rocks, and the Sun angle is used to derive the rock height.
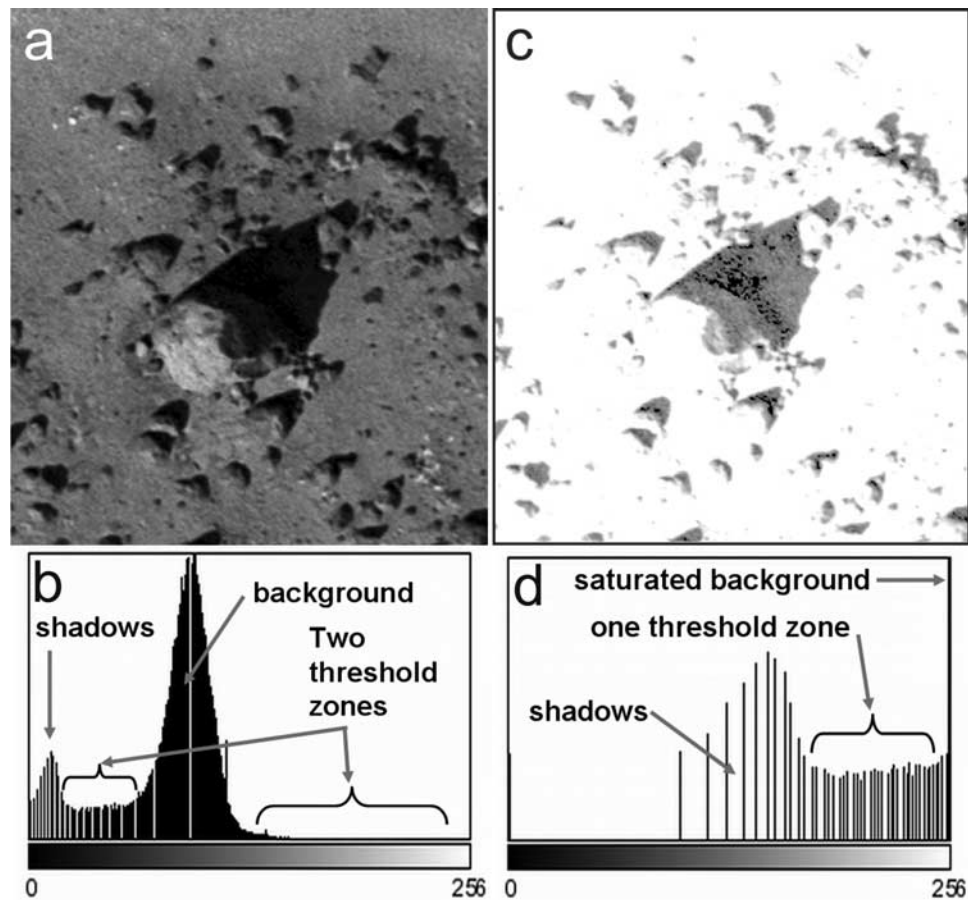
Figure 8. Segmentation of shadows using maximum entropy thresholding. (a) Illustrates the same large rock shown in Figure 7. (b) Simple thresholding of image intensities fails to identify one threshold that separates shadows. (c) Image after it has been gamma enhanced and segmented using the gMET algorithm. (d) The modified image histogram becomes strongly bimodal where the shadow intensities are spread and the nonshadow intensities are saturated. A single thresholding zone is identified, which segments the shadows from the rest of the saturated image.

tion of boulders is similar in slope to exponential model distributions derived from the Viking 1 and 2 landing sites, but are displaced to larger diameters. This is very similar to the size-frequency distribution determined for obvious boulders with sunlit and shadow sides in the equatorial region of Mars [*Golombek et al.*, 2003], all of which are difficult to relate to the model rock distributions based on rocks counted at the surface.

[9] Table 1 shows the results of the analysis of all 1624 boulder fields counted in 287 MOC images in regions A, B, and C. Boulder fields averaged 6 km^2 in area and covered 5.6% of the area covered by MOC images (and ranged from 2% in region A to 7% in region B). However, the area within each boulder field that was actually covered by boulders is only about 1% and the area covered by boulders out of all the area covered by MOC images is only a fraction of a percent. Boulder fields in MOC images were compared to areas covered by Thermal Emission Imaging System (THEMIS) visible images and 85% of areas with boulder fields in MOC images also appeared as dark areas in THEMIS images [*McGrane and Golombek*, 2006]. Even though region B had the greatest area covered by boulder
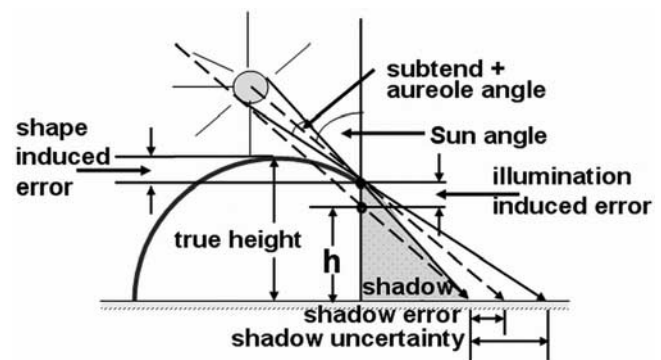

Figure 9. The Sun subtends an angle of 0.33° on Mars plus an aureole angle induced by forward scattering of light by the atmosphere. The variation in radiation flux induces a shadow penumbra where the direct to indirect illumination transition occurs. The gamma parameter setting during shadow segmentation manages this uncertainty with lower setting resulting in larger shadows. The height of rounded rocks is not fully represented by the shadows due to the rock shape and Sun angle.
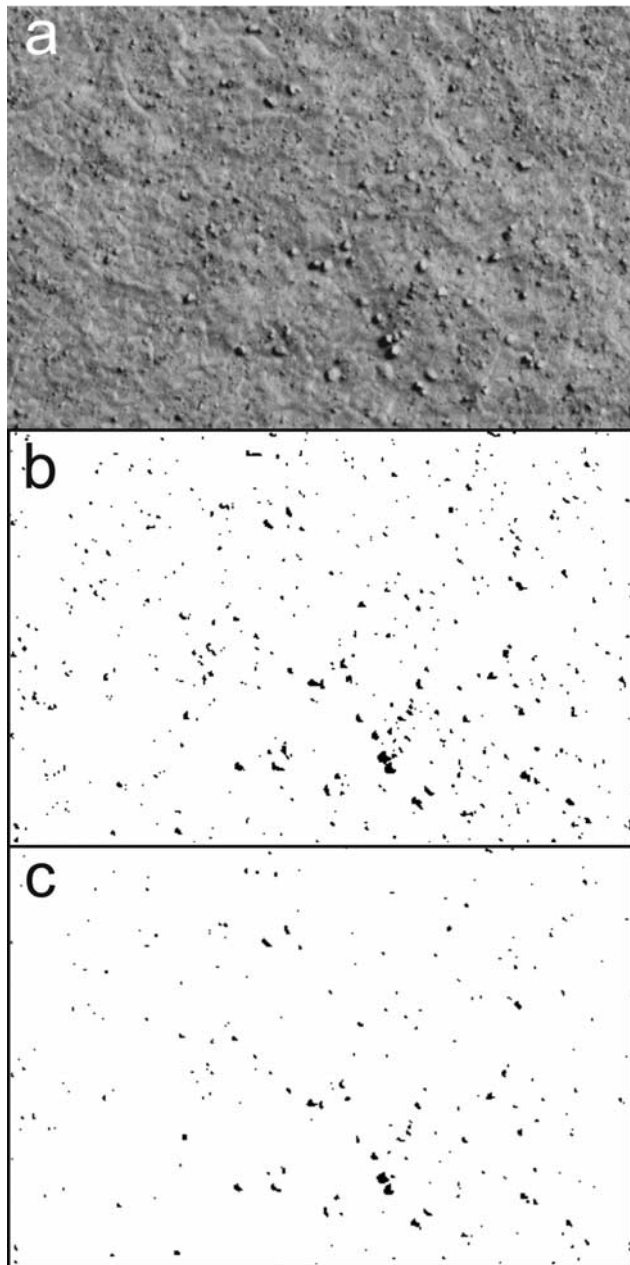
fields in MOC images, the area covered by boulders is so small that it remained the preferred region for landing Phoenix prior to the return of HiRISE images [*Arvidson et al.*, 2008].

3. Rocks in HiRISE Images

[10] Initial HiRISE images with higher resolution (~0.3 m/pixel) and an improved signal-to-noise ratio clearly showed that darker patches in MOC images are in fact fields of boulders [*McEwen et al.*, 2007b] with bright sunlit sides and dark shadows (Figures 4 and 5). Examination of MOC images in the preferred region B, prior to HiRISE images shows polygonal terrain and patterned ground (e.g., ''basketball terrain'') that is homogeneous across much of the northern plains surface [*Mellon et al.*, 2008; *Seelos et al.*, 2008]. As described in section 2, degraded crater rims and multiple-kilometer-scale polygon interiors often appear darker in these MOC images, but the spatial resolution is generally insufficient to confidently attribute the albedo variation to rocks in particular. Figures 4 and 5 illustrate typical terrains found in region B as they appear in both MOC and HiRISE images. Small dark patches in MOC images are most frequently resolved to be clusters of submeter boulders; rarely, individual dark pixels in MOC images map to individual boulders larger than ~2 m (see Figure 4, area B). Patches of relatively dark plains and the interiors of multiple-kilometer polygons seen in MOC images are revealed to consist of dense fields of boulders frequently greater than 1 m in diameter (Figure 5, area D). As a result, uncertainties from the lack of thermal constraints on the rock abundance and the inability to uniquely identify and resolve individual rocks in MOC data caused selection of areas that higher resolution HiRISE images showed are risky for landing Phoenix.

[11] To evaluate the effect that the clustering of rocks into dark groups of pixels in MOC images had on the measured

Figure 10. The effect of gamma enhancement of shadow segmentation. (a) The 441 × 298 pixel subimage from the HiRISE image PSP_001391_2465 spans an area of 136.7 m × 92.4 m. The image resolution is about 0.31 m/pixel. The illumination direction is from the upper right, and the Sun elevation angle is 31.5°. (b) A low gamma setting (3.5) has the effect of increased shadow region sizes as the regions include more pixels in the shadow penumbra (uncertainty zone in Figure 9). (c) The opposite results with higher gamma settings. The smaller shadow regions include less penumbra pixels. Gamma manages the effects of the atmosphere, the imager optics, and the sensor characteristics on the shadow segmentation.

Figure 11. Rock modeling from the shadows. Shadow regions are represented by best fit ellipses that preserve the area of the shadow. The length of the shadow is approximated by the length of the ellipse (axis is dashed line) projected onto the illumination ray (axis is solid line) and used in combination with the Sun incidence angle to estimate rock height. The rock is modeled as a cylinder, centered at the terminator, whose diameter is equal to the width of the shadow ellipse.

HiRISE images. Finally, HiRISE rock counts show portions of the cumulative fractional area distributions at large rock diameters are more parallel to the exponential model distributions than the MOC cumulative fractional area distri-
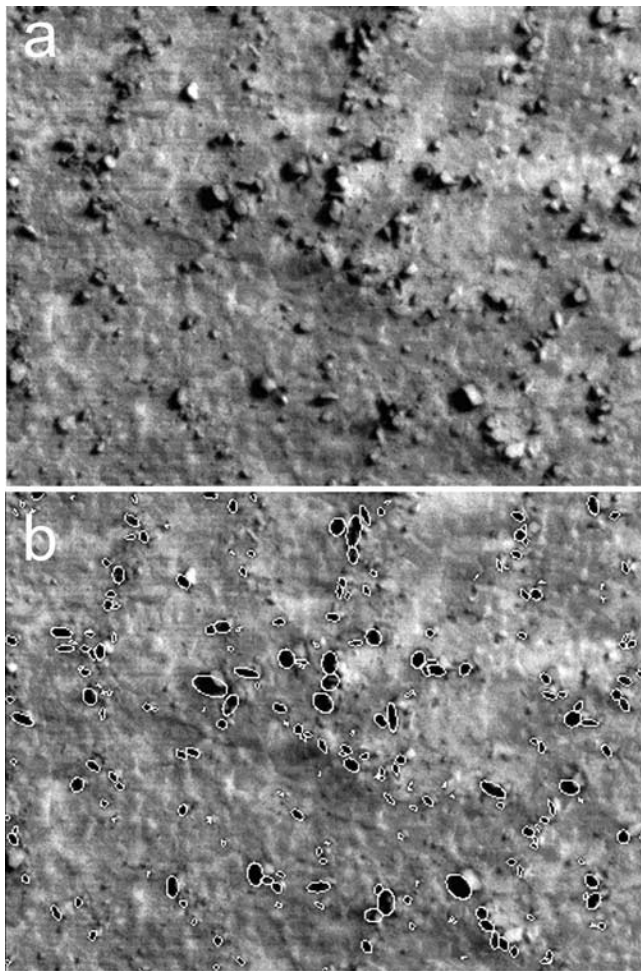

Figure 12. Area with large boulders showing ellipses modeled from the segmented shadows. The smallest estimated rock diameter is about 70 cm. (a) The subimage illustrates a 124 m × 93 m area of HiRISE image PSP_001880_2485. The image resolution is about 0.31 m/pixel. The direction of illumination is from the upper right and the Sun elevation angle is 33.3°. (b) The shadow regions (>5 pixels) approximated by ellipses overlaid on the image help to visualize two aspects of the automatic detection process. One is that shadow detection works quite well and does not miss rocks even if the rocks themselves are not clearly discernable. Another is that although the algorithm attempts to detect individual rocks by splitting merged shadows, there are a few cases where shadows are not split.

size-frequency distribution of rocks, counts were made of the same areas in MOC and HiRISE images shown in Figure 4, area B, and Figure 5, area D. The cumulative fractional area versus diameter plot in Figure 6 shows that the MOC boulder counts are at greater diameters for a given cumulative fractional area compared with the HiRISE counts, which is consistent with the visual comparison that shows that dark pixels in MOC images are really clusters of smaller rocks. In addition, the clusters of rocks measured in the MOC images generally elevates the total area covered by rocks over the measurement of individual rocks in the

Figure 13. Rocky area showing base circle of rock cylinders fit to rocks. (a) Image illustrates a 100 m × 100 m (one square hectare or 10,000 m²) subimage from HiRISE image PSP_001391_2465 (~0.31 m/pixel). The direction of illumination is from the upper right, and the Sun elevation angle is 31.5°. The largest shadow is about 9 pixels across. (b) The rock models are illustrated by circles placed at the estimated rock position. Rock circles are at the terminator and partially overlap the shadows. Shadows larger than 5 pixels in area are used to estimate rocks.

Table 2. Measurements of Lander or Rover Width and Height Derived From Automated Measurement of Shadows Cast ("Rocks")

Lander	HiRISE Image	Resolution (m/pixel)	Sun Elevation (deg)	"Rock" Diameter (m)	"Rock" Height (m)	Lander/Rover Width (m)	Lander/Rover Height (m)
VL1	PSP 1521	0.30	42.4	2.01	1.67	~2.7	~2.0
VL1	PSP 1719	0.29	40.0	2.18	2.22	~2.7	~2.0
VL2	PSP 1976	0.30	32.2	2.54	1.41	~2.7	~2.0
VL2	PSP 1501[a]	0.31	39.4	2.46	1.73	~2.7	~2.0
VL2	PSP 2055	0.33	32.9	2.61	1.64	~2.7	~2.0
MPF	PSP 1890	0.28	37.5	1.58	0.90	1.4[b]	0.9
MPF	PSP 2391	0.29	34.6	1.78	0.86	1.4[b]	0.9
MER A	PSP 1513	0.27	29.7	2.10	1.16	2.1[c]	0.65
MER A	PSP 1777	0.26	29.4	1.84	1.15	2.1[c]	0.65
MER A	PSP 2133	0.26	29.3	1.40	1.00	2.0[c]	0.65
MER B	PSP 1414	0.28	30.0	1.97	1.17	2.0[c]	0.65
MER B	PSP 1612	0.27	34.6	1.73	1.03	2.0[c]	0.65

[a]This image is blurred in places due to a mistaken "unpark" command to the high-gain antenna just before imaging, although the region around VL2 did not appear affected.
[b]Width of lander adjusted for solar illumination of base petal and lack of shadow produced by flat solar panel against ground.
[c]Width of rover adjusted for orientation of rover with respect to solar illumination.

butions before rolling off to shallower slope at diameters smaller than 1–2 m.

4. Automatic Rock Detection and Mapping

[12] In this section, we describe a tool for automatically detecting and measuring rocks in HiRISE images from shadows based on autonomous hazard detection and avoidance techniques developed for landing spacecraft [*Cheng et al.*, 2001, 2003; *Huertas et al.*, 2006, 2007; *Matthies et al.*, 2007]. The technique separates shadows cast by rocks from background terrain (shadow segmentation), fits an ellipse to the shadow and a cylinder to the rock, derives the rock diameter and height from these fits (Figure 7), determines the size-frequency distributions of rocks in the image, and produces maps of the cumulative fractional area or cumulative number of rocks larger than a given size per unit area. Following the receipt of the first HiRISE image showing northern plains surfaces littered with boulders, this technique was used to map the rock distributions over 1500 km^2 area and count more than 10 million rocks larger than 1 m in diameter during the Phoenix site selection process.

4.1. Shadow Segmentation

[13] The rock detector labels shadow pixels by applying a modified maximum entropy thresholding (gMET) algorithm [*Huertas et al.*, 2006] to find a threshold in the image histogram that separates shadowed from nonshadowed pixels. Using the classic definition of entropy, the uncertainty of the probability of a pixel gray level in the image is considered between two classes, shadows and nonshadows and the sums of their entropies. The gMET algorithm selects the threshold that maximizes the interclass entropy [*Kapur et al.*, 1985]. Histograms of gray level images, however, are not necessarily bimodal. In order to force bimodality, a gamma-corrected version of the image is added to the original image before creating a histogram to better segment the shadows from nonshadowed regions. Gamma correction, described in more detail in section 4.3, is a nonlinear image enhancement technique that stretches low intensities more than high intensities. Figure 8 illustrates the effect of shadow enhancement on the image histogram. The rock

surfaces and the soil are assumed to have similar reflectance and occupy the left half of the histogram (Figure 8b). If a scene includes distinctly brighter regions, the histogram would exhibit a third cluster on the right portion of the histogram. The dark regions are stretched ("looking into the shadows") in this operation and the remaining pixels are forced into a cluster at the bright end of the histogram.
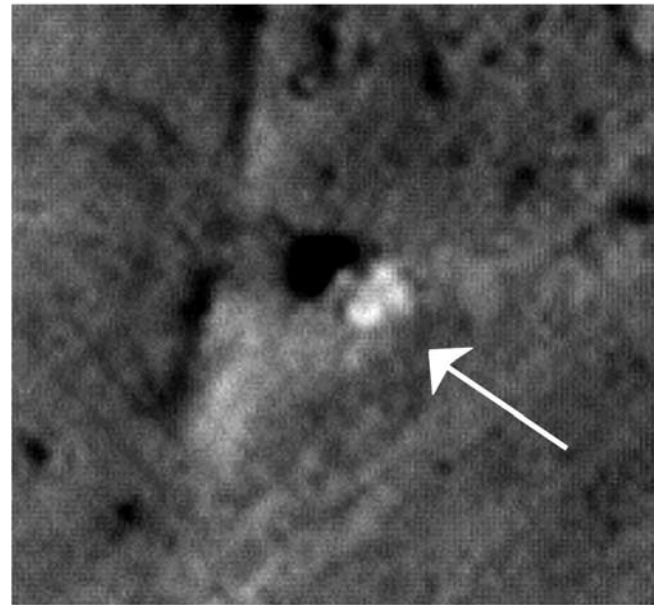

Figure 14. Portion of HiRISE image PSP 001513-1655 (27 cm/pixel) of the Spirit rover (229 cm wide and 151 cm long) near Home Plate on Mars. Solar azimuth of 150° shown by arrow. Judging by the shadow of the Pancam Mast Assembly beyond the shadow of the rover toward the northwest, the rover is oriented slightly counterclockwise of due north (up). The width of the solar panels casting the shadow in that orientation is about 211 cm, and the solar panels are 65 cm high. The rock detector determined the "rock diameter" to be 210 cm and the "rock height" to be 116 cm, in good agreement with the actual rover dimensions.
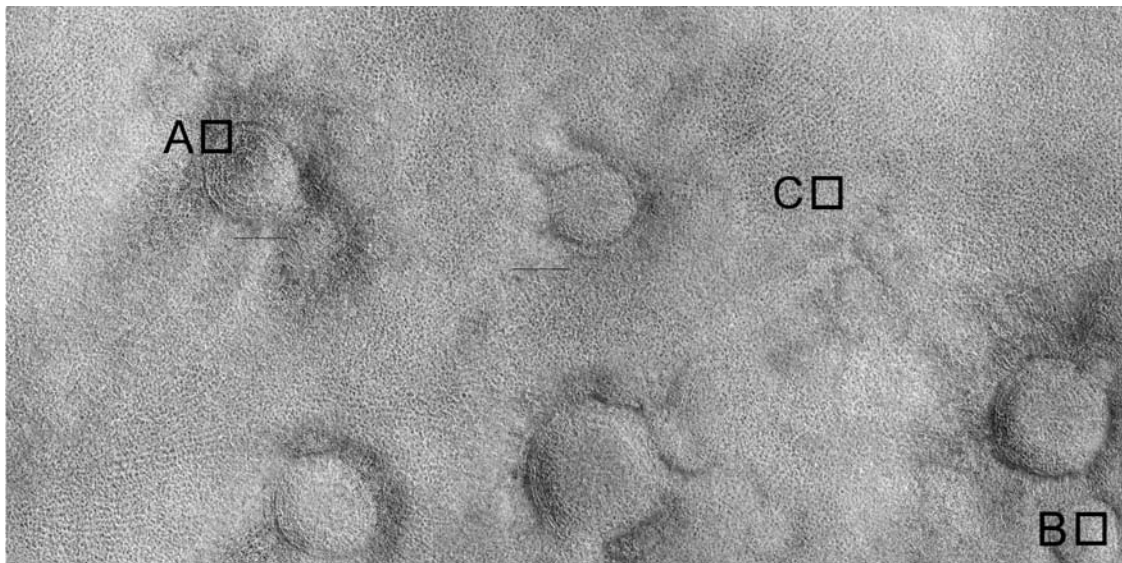
Figure 15. Transition orbit HiRISE image TRA_000828_2495 (0.31 m/pixel) of a portion of region B, the preferred area for landing Phoenix prior to the return of HiRISE images. Darker areas are produced by shadows from boulder and rock fields associated with highly degraded craters. Square areas denoted are shown in Figures 16a, 16b, and 16c. North is up; short axis of the image is about 6 km.

4.2. Shadow Geometry

[14] Errors and uncertainties in determining the rock height from the shadow cast by a rock are illustrated in Figure 9 for the worst case rock shape, a hemisphere. The sun subtends an angle proportional to its distance, about 0.5° on Earth and 0.33° on Mars. Forward illumination scattering from particles in the atmosphere induces a shadow penumbra where the direct to indirect illumination transition occurs. The width of the shadow is equivalent to the width of the rock, and the accuracy of its measurement will have up to one random pixel error. The length of the shadow, used to estimate height, is on the other hand, dependent on the Sun aureole angle and on the height of the rock. The shadow penumbra represents an interval of uncertainty in the farthest shadow point from the rock. In the ideal case, the shadow is cast on flat level ground and the correct shadow point occurs halfway along the penumbra. For red band-pass HiRISE images and typical atmospheric scattering on Mars (see section 4.3 discussion) the shadows span a few pixels and all these effects are combined within one pixel. The height estimate, however, is also dependent on the shape of the rock. As Figure 9 indicates, even if the length of the shadow can be measured accurately, the farthest shadow point is not necessarily the highest point on a hemisphere rock. Rock heights are thus slightly underestimated for hemisphere shaped rocks and would be more accurate for angular topped rocks. Correcting the derived rock height for the shape of the rock top is possible from the shape of the shadow boundary, but would require much higher resolution images than HiRISE for rocks smaller than a few meters diameter and so is not attempted herein.

4.3. Shadow Enhancement: Gamma

[15] Because the rock detection algorithm was originally developed to run in real time during descent and landing, all factors affecting image quality (e.g., sharpness, contrast, and noise) as well as atmospheric aerosols and attenuation are compensated for by a single parameter called gamma, a nonlinear image enhancement technique that stretches lower intensities more than higher intensities. Experimentation with Mars Exploration Rover surface images and HiRISE orbital images of materials with a wide variety of albedos and optical depths shows that red images offer the greatest contrast and that shadows cast are easily distinguished for optical depths of less than 0.8, no significant condensate hazes, and solar elevations of less than 60°. Low gamma stretches yield the most extended shadows as the boundary of the shadow approaches the outer edge of the penumbra. Experience in processing red HiRISE images shows lower values of gamma include more of the smaller boulders and partially ameliorates the underestimation of rock height (Figure 10).

[16] Gamma settings were set manually while processing the images and varied from 2 (little enhancement) to 6, depending on image contrast and sharpness. Lower contrast images and small rocks (few pixels in diameter) require lower gamma values. For high contrast images and large rocks (tens of pixels) higher values are appropriate (Figure 10). In processing the HiRISE images, the number of shadow pixels for an image was evaluated for different gamma values and set where the number of shadow pixels begins to rapidly decline. Shadow regions that are at least 5 pixels in area were processed, which favored gamma values in the range 3–5. Shadows that merge together from closely spaced rocks covering areas of more than 10 pixels were separated by first identifying the darkest core of the shadow as individual rocks and then adding back the adjacent lighter atmospherically diffused regions. Future improvements in the technique include applying the point spread function correction to the high signal-to-noise HiRISE images [e.g., *Kirk et al.*, 2008] prior to shadow

segmentation, which should allow counts to smaller rock diameters.

4.4. Shadow Analysis and Rock Modeling

[17] For each shadow, the program fits a ''best'' ellipse [*Cramer*, 1999] whose area is roughly the area of the shadow and whose length is the length of the shadow as shown in Figures 11 and 12. Next the program fits a circle or cylinder at the center of the rock terminator whose diameter is the width of the ellipse (Figures 11 and 13). From these fits, rock diameter is the diameter of the fitted circle and rock height is determined from the shadow length (length of shadow ellipse) and the solar elevation. For each detection, the location of the rock, the area, width, and length of the shadow are recorded as well as the rock diameter and height. To derive rock statistics and size-frequency distributions, the area of the image analyzed by the rock detector is recorded. This allows determination of the fractional area covered by rocks or the number of rocks binned over subareas that can be converted into rock density and thematic maps. In addition, the cumulative number of rocks larger than a given diameter or the cumulative fractional area of rocks versus diameter can be determined for the entire image or subareas.

4.5. Rock Detector Performance

[18] The rock detector algorithm has been extensively tested on Earth and on HiRISE images of Mars. Aerial images of Mars Hill in Death Valley, California, which has been measured as an Earth analog for the Viking landing sites [*Golombek and Rapp*, 1997], with different Sun elevations between 30° and 70° were used and compared with actual rock heights and diameters. Results show that the rock detector defines rock diameter and height from the images within about 5% of their true measurements [*Matthies et al.*, 2007]. In addition, a number of experiments were conducted for rock height estimation using an experimental setup that varied image distance and resolution for rocks of tens of centimeter diameter. Results show that errors in diameter observed using the rock detector software are on the order of one pixel [*Matthies et al.*, 2007].

[19] At the beginning of HiRISE image acquisition of potential Phoenix landing sites, rock diameter (the maximum width of the shadow) and shadow length were measured by hand [*Arvidson et al.*, 2008]. Later, the rock detector software was used to identify and count rocks of the same areas counted by hand. First, visual inspection of the ellipses fit to the rock shadows (Figure 12) and cylinders fit to rocks (Figure 13) in HiRISE images indicate reliable
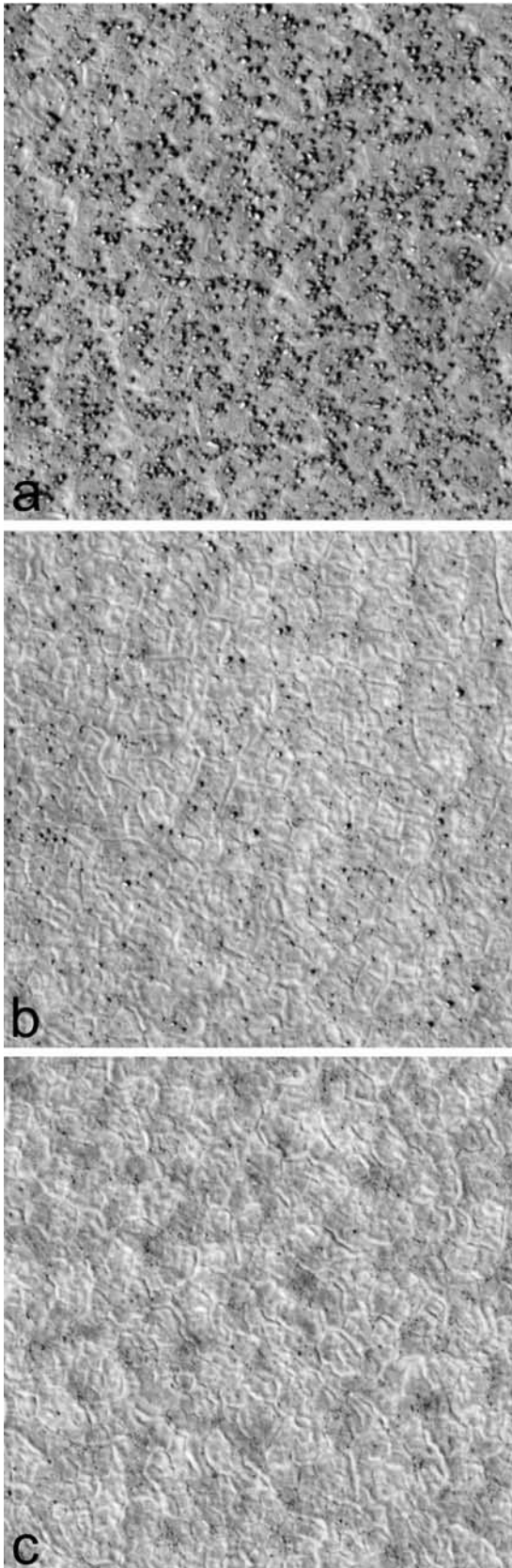
Figure 16. Portions of areas denoted in Figure 15. Images are 189 m across, 0.31 m/pixel, and cover 35,720 m^2 area. (a) Area A showing very rocky portion of HiRISE image. Rocks are clearly distinguished with bright sunlit sides and shadows cast. One thousand one hundred sixty two rocks were counted. (b) Area B of moderately rocky area denoted in HiRISE image. One hundred sixteen rocks were counted. (c) Area C of sparsely rocky area denoted in HiRISE image. Eleven rocks were counted.

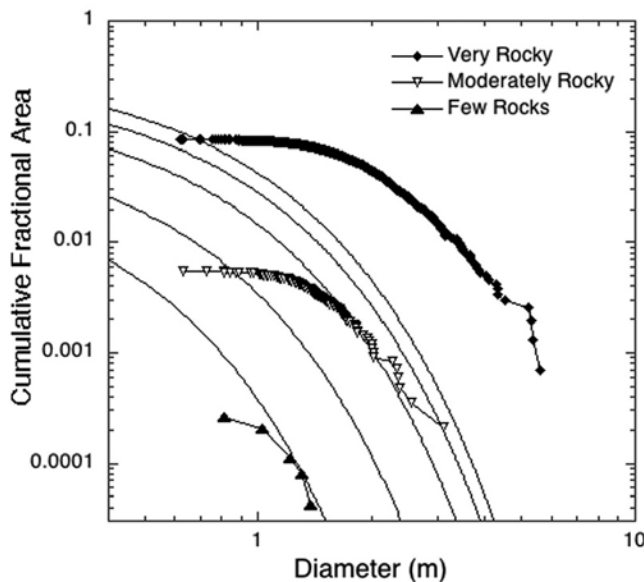**Figure 17.** Cumulative fractional area covered by rocks versus diameter for three areas shown in HiRISE image TRA 00828-2495 in Figure 16 (very rocky, moderately rocky, few rocks) in region B. Also shown from left to right are exponential model curves for cumulative fractional area rock coverage of 5%, 10%, 20%, 30%, and 40%, from left to right, respectively.

detection and fits. Next, the size-frequency distributions of about 4000 rocks in HiRISE test images derived via hand counts and the rock detector are indistinguishable, indicating that the rock detector is yielding results consistent with hand counts (see discussion of VL2 in section 7.2). Finally,

we compared the rock detector performance by measuring the width and height of shadows cast by landers and rovers on the surface in HiRISE images. Because the spacecraft have known dimensions, comparing them with the rock detector provides the ultimate "ground truth."Results for twelve HiRISE images of the landers and rovers are shown in Table 2. Adjusting the width of the rovers (Figure 14) and the Pathfinder base petal with respect to their orientation and solar illumination angle, the rock detector determined the width of the lander to within 1 pixel 8 times and within 2 and 3 pixels 2 times each. The rock detector measured the height of the lander or rover to within 1 pixel 4 times and to within 2 pixels 8 times. As expected, rock height was measured less accurately than rock diameter (see discussion in section 4.3). Even with these uncertainties, the rock detector is generally accurate to within $1-2$ pixels, which is about the limit of what could be expected. These results also argue that the modified Maximum Entropy Thresholding (gMET) algorithm for segmenting the rock shadows and the gamma enhancement technique are also not introducing any other large uncertainties and are adequately accounting for environmental parameters such as albedo differences and diffuse illumination due to dust in the atmosphere.

5. Rock Size-Frequency Distributions in HiRISE Images

[20] The first HiRISE images of region B, the preferred region for landing Phoenix prior to the return of HiRISE images, were returned during the transition orbit. Image TRA_00828_2495 shown in Figure 15 shows fairly common northern plains surface with few fresh impact craters, polygonally fractured ground and fields of dark rocks and boulders that appear to describe the rims and near ejecta of
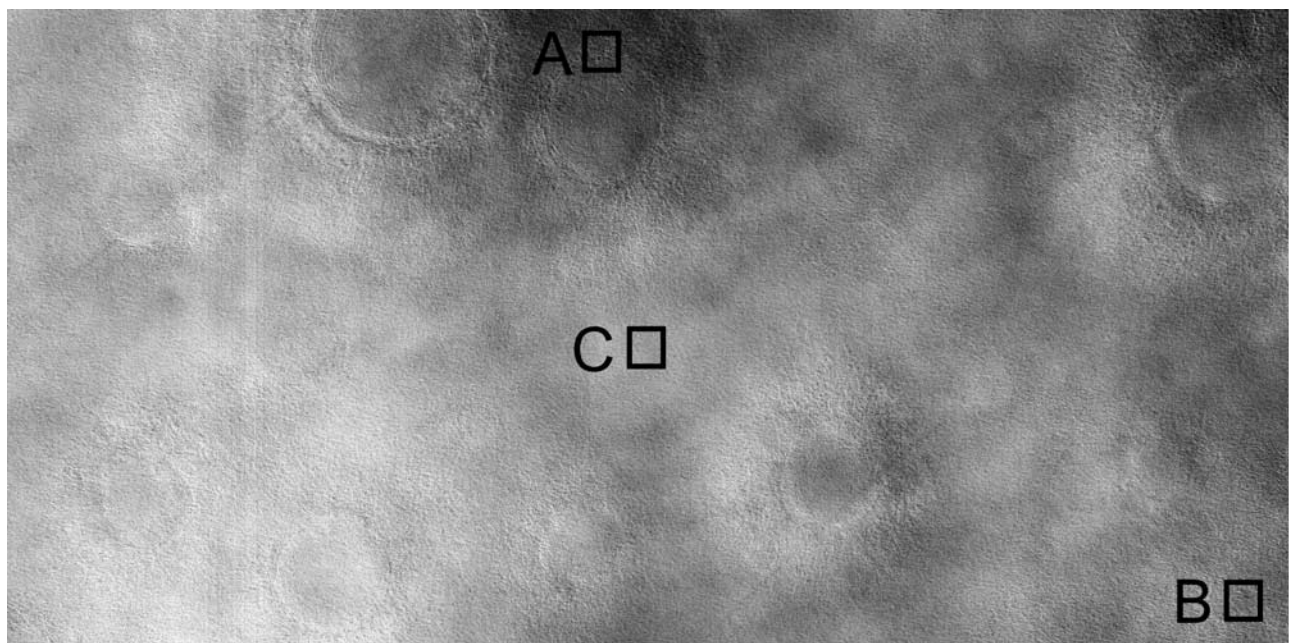

Figure 18. HiRISE image (PSP_001391_2465) of a portion of region A. Note darker areas are shadows produced by boulder and rock fields. Areas in boxes A, B, and C are shown in Figure 20. Image is 6.2 km wide and 0.31 m/pixel. North is up.
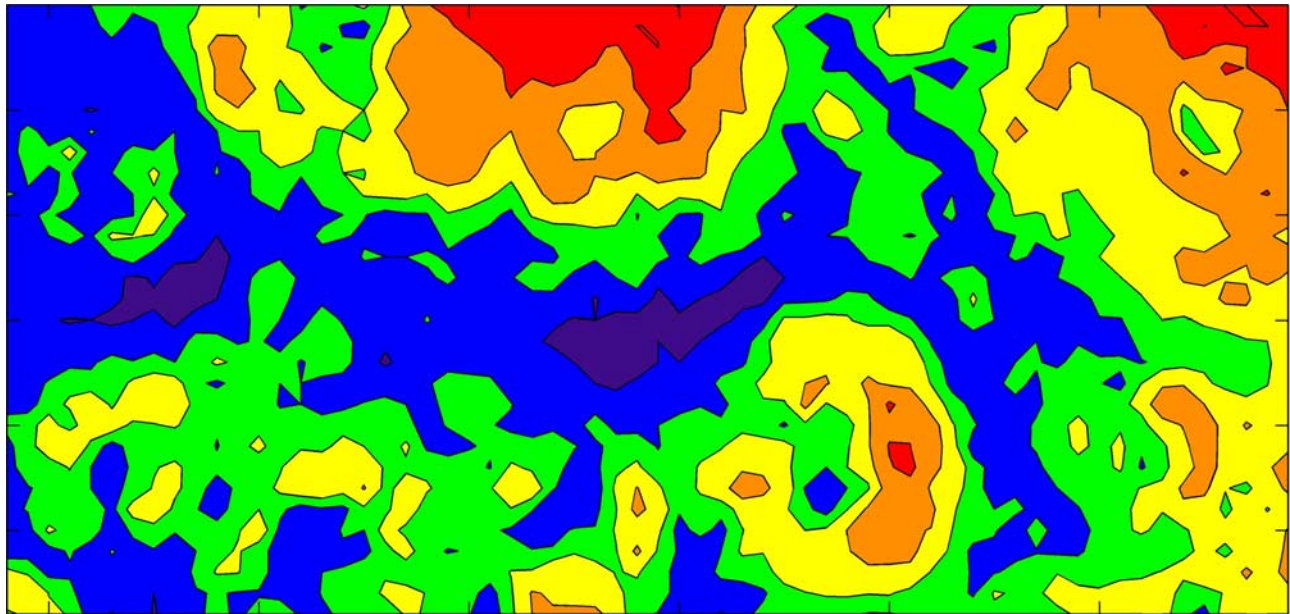
Figure 19. Thematic map showing total number of rocks per square hectare of 0–4 (dark blue), 5–16 (light blue), 17–32 (green), 33–64 (yellow), 65–128 (orange), and >129 (red) of HiRISE image shown in Figure 18. Ticks at bottom and top of image are 1 km apart; ticks at the sides are 0.5 km apart.

otherwise highly degraded impact craters. To first order, these fields of rocks and boulders appear similar to how they look in MOC images, but the higher resolution HiRISE images resolve individual rocks with sunlit bright sides and dark shadows. The darker areas in the HiRISE images have higher concentrations of rocks (Figure 16a) and have a more neutral (less red) color compared with lighter areas that have fewer rocks (Figures 16b and 16c).

[21] A plot of the cumulative fractional area covered by rocks versus diameter is shown in Figure 17 for areas with high, medium and low densities of rocks. The distribution of rocks in areas with few rocks generally parallels the exponential model distribution (described in section 1) for 5% rock coverage for diameters larger than about 1.1 m, but falls below the curve for smaller diameters. A similar drop off in the cumulative fractional area of rocks occurs for small diameter rocks for medium and high rock density areas, except that the roll-off occurs at slightly larger rock diameter (∼1.5 m for medium density areas and ∼2 m for high-density areas). Areas with medium densities of rocks have cumulative fractional area distributions that parallel the model curves for 20% rock coverage. Very rocky areas have cumulative area distributions that fall well to the right of model distributions of 40% rock coverage, but are generally parallel to the models while appearing to roll over at larger diameters than areas with fewer rocks. Very rocky areas have extreme rock coverage with ∼5% of the surface covered by 2 m or larger rocks. If extended roughly parallel to the model distribution approximately half of the surface would be covered by rocks 0.4 m or larger, which appears consistent with the rock coverage in Figure 16a. What happens to the distribution at smaller diameters is not clear, but if extended to 0.02 m diameter, rocks could cover ∼90% of the surface. The largest rock in these distributions increases as the density of rocks increases from 1.4 m, to

3 m, and to 5.5 m diameter for the 5%, 20% and extreme distributions shown.

[22] Similar distributions of rocks were found throughout the northern plains of Mars. Figure 18 shows a HiRISE image of a portion of region A (PSP_001391_2465) with gradients in tone that are related to the density of rocks with the dense rock fields associated with very degraded impact craters. The rock detector counted all rocks in this HiRISE image and mapped areas with concentrations of rocks that are 0–4 (dark blue), 5–16 (light blue), 17–32 (green), 33–64 (yellow), 65–128 (orange), and >128 (red) rocks per square hectare or 10,000 m^2 area in Figure 19. Representative areas with rock concentrations of >128, 33–64, and 0–4 rocks are shown in Figures 20a, 20b, and 20c, respectively. The size-frequency distribution of rocks in these areas is shown in Figure 21 and shows the cumulative number of rocks that parallel the exponential models for ∼5%, ∼12%, and ∼30% rock coverage for the low, medium and high rock abundance areas. As observed in other plots, the roll-off where the distributions begin to fall below the models increases from <1 m to 1.2 m to 1.5 m diameter, and the largest rock increases from 1.6 m to 2 m to 3.3 m diameter as the density of rocks increases for the three distributions.

[23] The size-frequency distribution of all rocks in HiRISE image PSP_001391_2465 grouped into 0–4, 5–16, 17–32, 33–64, 65–128, and >128 rocks per hectare concentrations are plotted in Figure 22. The cumulative number of rocks for areas with 0–4 rocks per hectare parallels the exponential model distribution for 5% rock coverage for rock diameters 2 m to 1.1 m and then falls below the model at smaller diameters. Areas with 5–16 rocks per hectare have distributions that parallel the model for ∼8% rock coverage for rock diameters 3 m to 1.3 m and then falls below the model at smaller diameters. Similar character cumulative number distributions are found
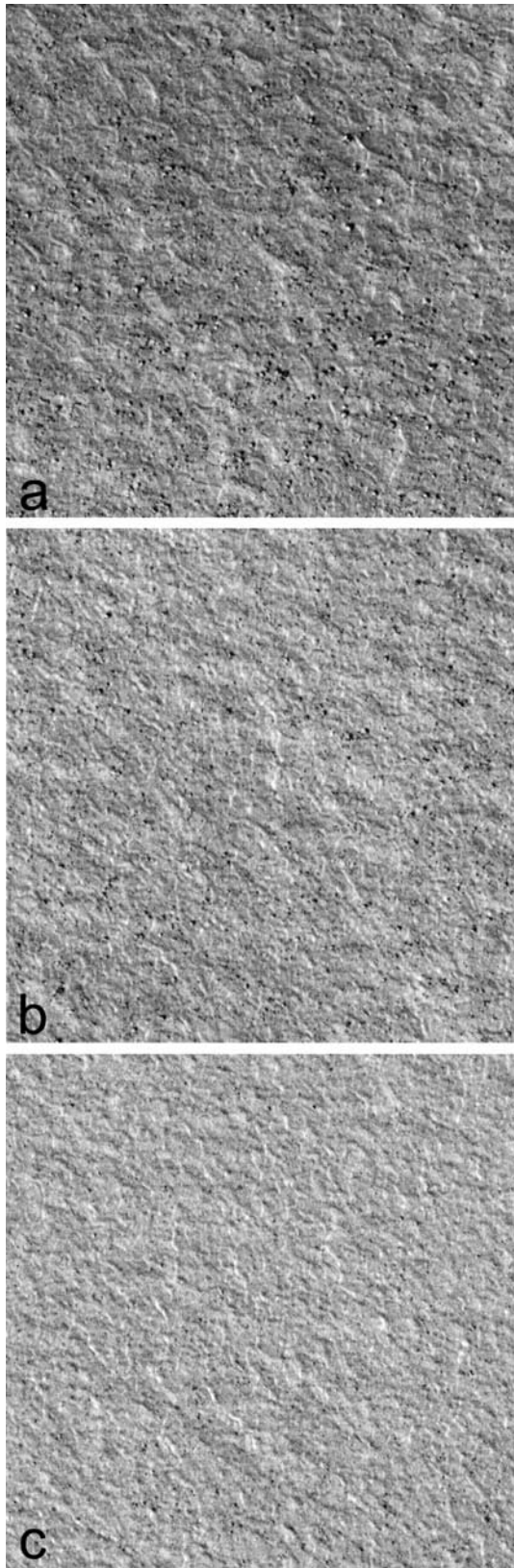
for areas with 17–32, 33–64, 65–128, and >128 rocks per hectare that parallel models for 10%, 15%, 20% and 40% rock coverage for rock diameters 3.5–1.3 m, 4.1–1.5 m, 4.5–1.3 m, and 4.6–1.6 m, respectively.

[24] HiRISE-based rock distribution measurements show the same relationships throughout the northern plains as illustrated in the examples shown. Rock distributions at large rock diameters parallel exponential models for cumulative fractional area covered by 5% to 90% rocks, where the greatest density of rocks in fields around craters have 30–90% rock coverage, less dense fields around craters have 10–30% rock coverage, and background terrain away from craters have 0–10% rock coverage. At rock diameters between 1 and 2 m, HiRISE distributions flatten considerably well below lander rock distributions or the models. This appears similar to a resolution roll-off (common in crater counts) [e.g., *Wilhelms*, 1987], where it become difficult to recognize all objects less than about 5 pixels across [*Bourke*, 1989]. The same general relationships are found in cumulative fractional area covered by rocks versus diameter plots (e.g., Figure 6), where measured distributions fall off below model curves below 1–2 m diameter. The tendency of the rock distributions of areas with higher concentrations of rocks to roll-off at slightly higher diameter may be related to difficulties in observing all rocks near the resolution limit when there are so many rocks. Because the model curves were derived from Viking lander rock distributions at diameters from 2 cm to about ~1 m, the observation that rock distributions measured at diameters greater than 1–2 m parallels these models suggests that both the lander and HiRISE distributions are part of the same population and that the roll-off with decreasing diameter is a function of resolution. Finally, because the rock detector

Figure 20. Areas in boxes A, B, and C shown in Figure 18 (images are 186 m across, 0.31 m/pixel). (a) Area of >129 rocks per square hectare (red); 404 rocks were counted. (b) Area with 33–64 rocks per square hectare (yellow); 124 rocks were counted. (c) Area of 0–4 rocks per square hectare (dark blue); 13 rocks were counted.
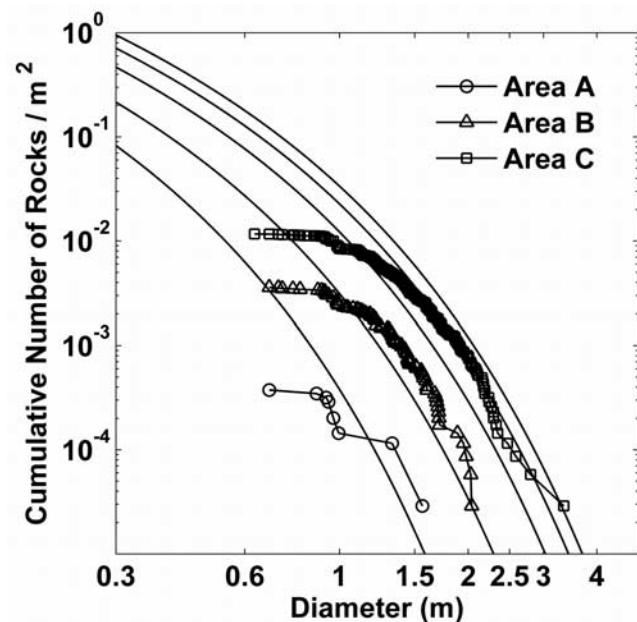

Figure 21. Cumulative number of rocks per m² versus diameter of three areas shown in Figure 20. Also shown from left to right are model curves for cumulative fractional area rock coverage of 5%, 10%, 20%, 30%, and 40%, respectively.
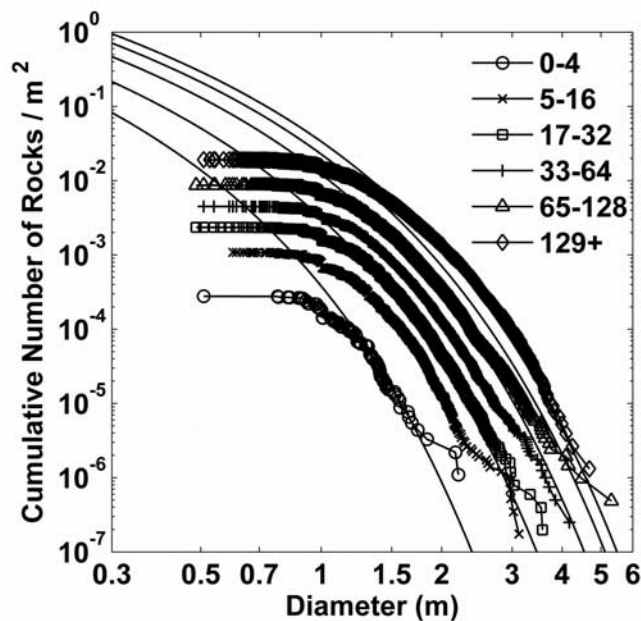
Figure 22. Cumulative number of rocks per m^2 versus diameter of all rocks counted in Figure 19 binned by total number of rocks per square hectare (colors refer to rock densities mapped in Figure 19). Dark blue areas have 0–4 rocks per hectare; 253 rocks were counted in 0.91 km^2. Blue areas have 5–16 rocks per hectare; 5817 rocks were counted in 5.74 km^2. Green areas have 17–32 rocks per hectare; 11,901 rocks were counted in 5.05 km^2. Yellow areas have 33–64 rocks per hectare; 14,993 rocks were counted in 4.0 km^2. Orange areas have 65–128 rocks per hectare; 17,973 rocks were counted in 2.06 km^2. Red areas have >129 rocks per hectare; 14,533 rocks were counted in 0.76 km^2. Also shown from left to right are model curves for cumulative fractional area rock coverage of 5%, 10%, 20%, 30% and 40%, respectively.

software also determines the height of the rocks from the length of the shadows, extensive comparisons of rock height versus diameter have been made for all of the counts. Results show that rock height is overwhelmingly about half of the rock diameter, a result similar to that found from lander rock counts [*Golombek and Rapp*, 1997; *Golombek et al.*, 2003], so that rocks can generally be treated as hemispheres for hazard assessment.

6. Comparison of Lander and HiRISE Rock Counts

6.1. Introduction

[25] The best way to determine if the rock distributions measured in HiRISE images are part of the same population observed at smaller diameter from lander images is to compare them to results obtained by analyzing HiRISE images. Of the 5 landing sites where spacecraft have returned data, three have relatively high rock abundances (VL1, VL2, and MPF) as estimated from thermal differencing techniques in orbital data [*Christensen*, 1986; *Nowicki and Christensen*, 2007] and from measurements on the ground [e.g., *Golombek et al.*, 2008]. The cratered plains

at Gusev crater have rock abundance near the global average (∼8%) [*Golombek et al.*, 2006] and have few rocks visible in HiRISE images, except in locally rocky ejecta deposits around craters. Meridiani Planum has few rocks on the ground as indicated by orbital estimates [*Golombek et al.*, 2005]. Rock abundances from thermal observations are 16–18% for VL1, VL2 and MPF from Viking [*Christensen*, 1986] and 13 ± 4%, and 12 ± 4% at VL2 and MPF, respectively, from TES [*Nowicki and Christensen*, 2007]. Rock abundance estimates from lander images are 16–19%, even though the spatial scale of the orbiter observations is ∼60 km for Viking and ∼3 km for TES, and the landers are on the order of only 10 m [*Moore and Keller*, 1990, 1991; *Golombek et al.*, 2003, 2005]. In this section, rock distributions counted in HiRISE images are compared directly to distributions measured from lander images at the 3 landing sites with relatively high rock abundances (VL2, VL1 and MPF).

6.2. Viking Lander 2

[26] The first lander imaged by HiRISE was of VL2 that was returned in late November 2006. This site was selected because it is a high northern latitude site (47.6° N) that in available remote sensing data looked similar to areas under consideration for landing Phoenix [*Arvidson et al.*, 2008; *Seelos et al.*, 2008]. Available high-resolution (∼3 m/pixel) Mars Orbiter Camera (MOC) images showed surfaces near VL2 to be relatively flat with "basketball" texture terrain composed of small nubbins or light, dark speckling similar to the nubbly surface of a basketball and like many surfaces in the arctic northern plains of Mars. Other surfaces nearby VL2 and in the high northern plains are characterized by small polygons that were identified from the lander [*Mutch et al.*, 1977] and have been argued to be analogs to ice wedge polygons in permafrost regions on Earth [*Mellon et al.*, 2008].

[27] A portion of the first HiRISE image of VL2 is shown in Figure 23. Figure 23 shows a rocky plain with lighter toned polygons. The lander is clearly visible in the center of Figure 23 with two bright spots that correspond to the two wind covers over the radioisotope thermoelectric generators. The lander casts a distinct shadow (solar elevation 39°). The Viking landers were constructed in a way that allowed stereo imaging of the surface within 3 m in only one direction in an area known as the "near field" that could be accessed by the lander arm [*Moore et al.*, 1987] partly shown in Figure 24. Figure 24 shows a rocky plain that extends from the far edge of the "near field" to the "far field" where stereo measurements could still be reliably made [*Moore and Keller*, 1990, 1991]. The 7 largest rocks (0.6–0.9 m diameter) measured in the near and far field are labeled in Figure 24, and the soil filled trough that corresponds with the light polygon in the HiRISE image toward the northeast is clearly shown. The surface material map produced from the lander stereo images showing all rocks reliably counted with stereo images within around 10 m [*Moore and Keller*, 1991] is superimposed on a portion of the HiRISE image immediately around the lander in Figure 25 with the same 7 largest rocks in Figure 24 identified. Figure 25 clearly shows that the same rocks visible from the lander show up as bright dark pairs of
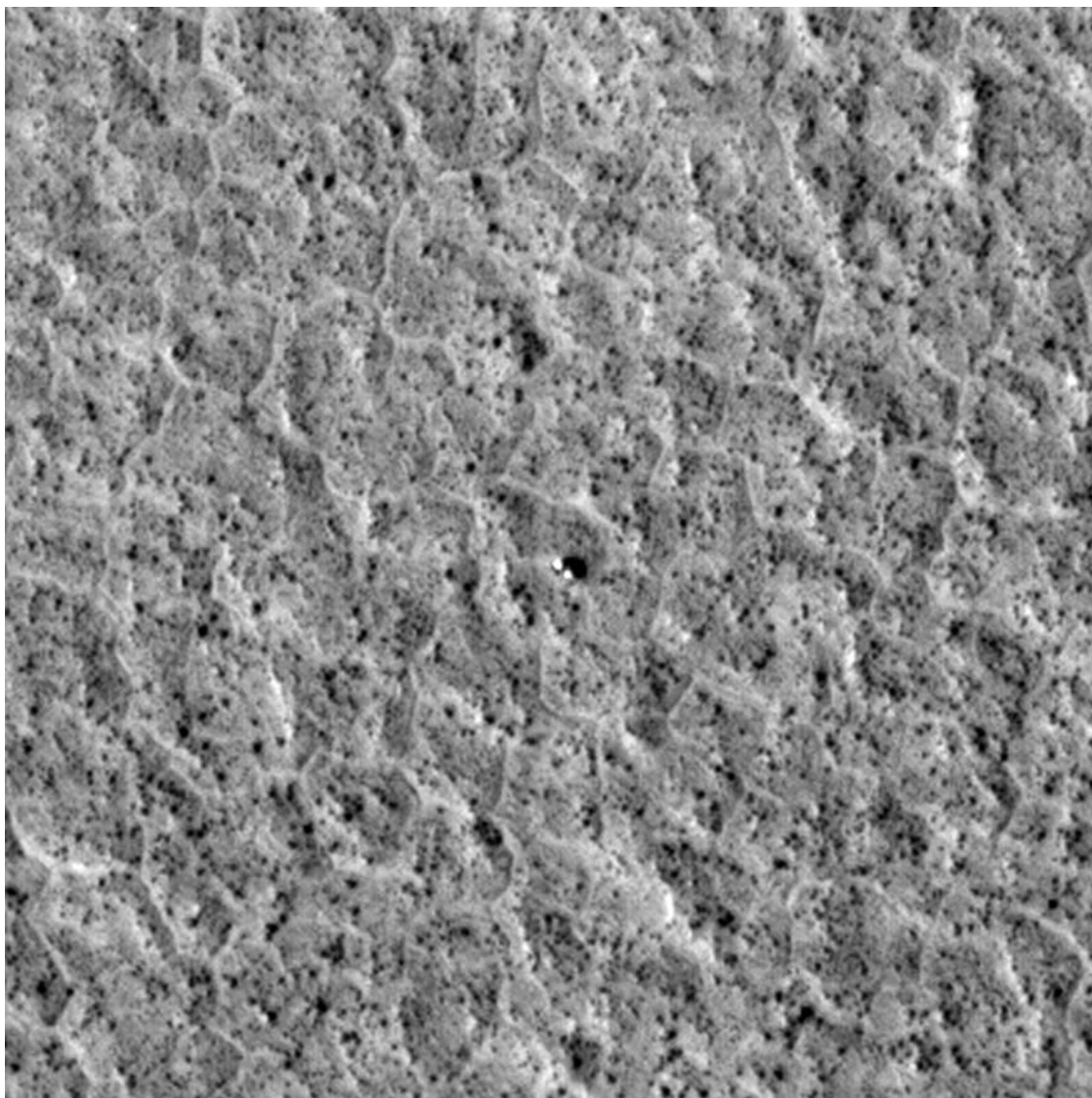
Figure 23. HiRISE image of rocky plain and Viking Lander 2 in Utopia Planitia. Area shown is 124 m across with north up. Lander is about 2.7 m across and 2 m high. Dark spots are shadows of rocks that were counted; note lighter polygons. HiRISE image PSP_001501_2280 is 0.25 m/pixel with Sun from the southwest at an elevation of 39°.
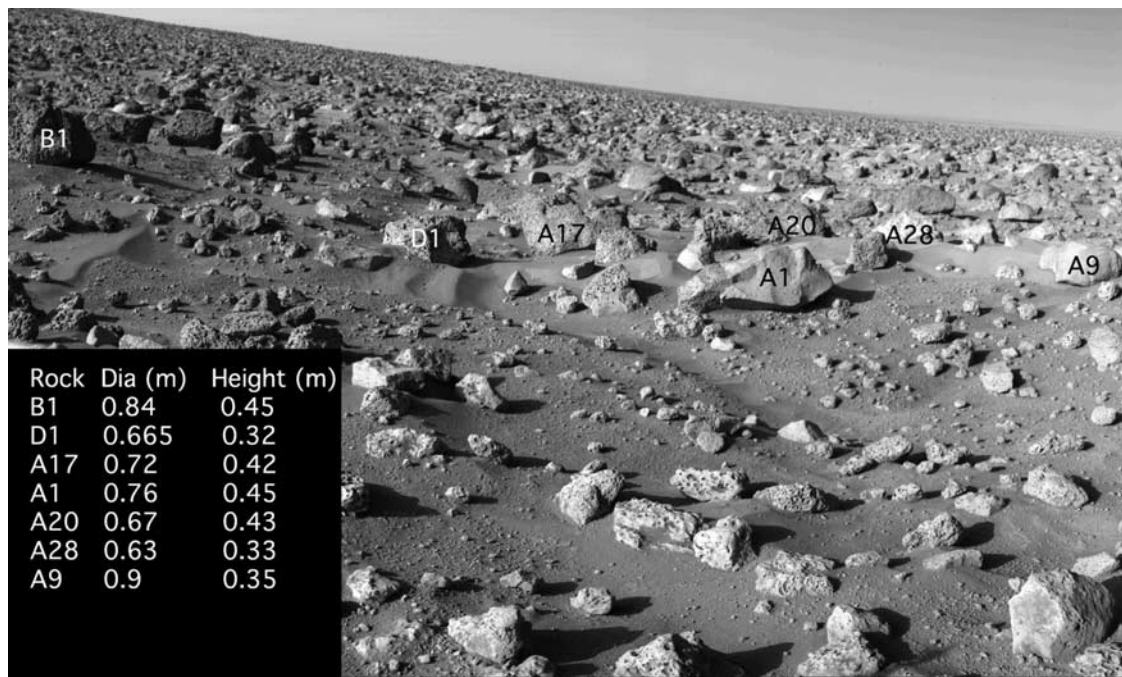
Rock	Dia (m)	Height (m)
B1	0.84	0.45
D1	0.665	0.32
A17	0.72	0.42
A1	0.76	0.45
A20	0.67	0.43
A28	0.63	0.33
A9	0.9	0.35

Figure 24. Viking Lander 2 image looking toward the northeast in the direction of the sampling area (nearby areas in other directions are blocked from view by the lander). Area shown extends from the far end of the sample area or "near field" (within reach of the arm) about 2 m from the lander to the horizon. The seven largest rocks measured from the lander are in the "far field" (beyond the sample area) labeled as shown by *Moore and Keller* [1991]. The closest of these large rocks, A1, is about 5 m from the lander; the farthest, B1 and A20, are about 9 m from the lander imagers, which is at about the limit of the stereo capability. Note soil-filled trough that extends across the scene, which corresponds to the bright polygon in the HiRISE image.

pixels corresponding to the sunlit side and shadowed area behind each rock.

[28] Rock counts of 24,025 m^2 area centered on VL2 (slightly larger than the area shown in Figure 23) were performed in three HiRISE images and are illustrated in Figure 26. The automated counts yielded about 300 rocks between about 3 m diameter and 0.5 m diameter (about 2 times the pixel scale). Also shown is a hand count of the shadow width over a similar area that extends down to about a single pixel. The size frequency distribution shown from the 3 images are virtually identical, indicating the automated rock counting algorithm is both highly repeatable and is virtually identical to the hand count as discussed in section 4.5. The cumulative number of rocks larger than a given diameter per meter squared versus diameter parallels the 30% exponential model cumulative fractional area curve at diameters greater than about 1.5 m and varies from around 10^{-4} to 10^{-2} rocks/m^2. At smaller diameter (∼1.5 m) the counted rocks fall below the model. Rock counts from the VL2 lander near and far field shown in Figure 25 over ∼84 m^2 [*Moore and Keller*, 1991] parallel the 20% model cumulative fractional area curve and vary from 0.01 to 5 rocks/m^2 for diameters of 1 m to 5 cm. The distributions show that the largest rock from the lander images (about 0.9 m) falls directly on the distributions measured from HiRISE. Further, the continuity of these distributions indicate that both the HiRISE and landed counts are sampling the same distribution of rocks and that the roll-off in the HiRISE distributions below about 1.5 m

diameter is a function of resolution. This is similar to the resolution roll-off found in crater counts in which not all craters are measured as the diameter of the crater approaches the resolution or detection limit of the image. The roll-off in the HiRISE counts is roughly at the expected diameter of about 1.5 m, as experience has shown that about 5 pixels are required to confidently identify objects [e.g., *Bourke*, 1989]. The difference in rock coverage at the HiRISE (30%) versus lander (20%) counts is likely a sampling effect from the very different areas counted. Visual comparison of the area counted from the lander with other areas in the HiRISE image indicates a variation of ±10% rock coverage is easily obtained by moving the smaller lander counting area around in the image. These results from VL2 demonstrate that rock distributions on Mars can be extrapolated along model curves to smaller diameters from counts in HiRISE images and show that for the first time that high-resolution images from orbit are sampling the same population of rocks as observed from the landers.

6.3. Viking Lander 1

[29] Viking Lander 1 was the second lander imaged by HiRISE, which shows a rougher but much less rocky surface (Figure 27) than VL2. The total number of rocks counted in a similar area is substantially fewer (about one third) than for VL2. Unlike VL2 no large rocks are present in the "near or far field" of VL1 [*Moore and Keller*, 1990] and none are visible in the HiRISE image. The largest rock near the lander is Big Joe, which is about 10 m away and
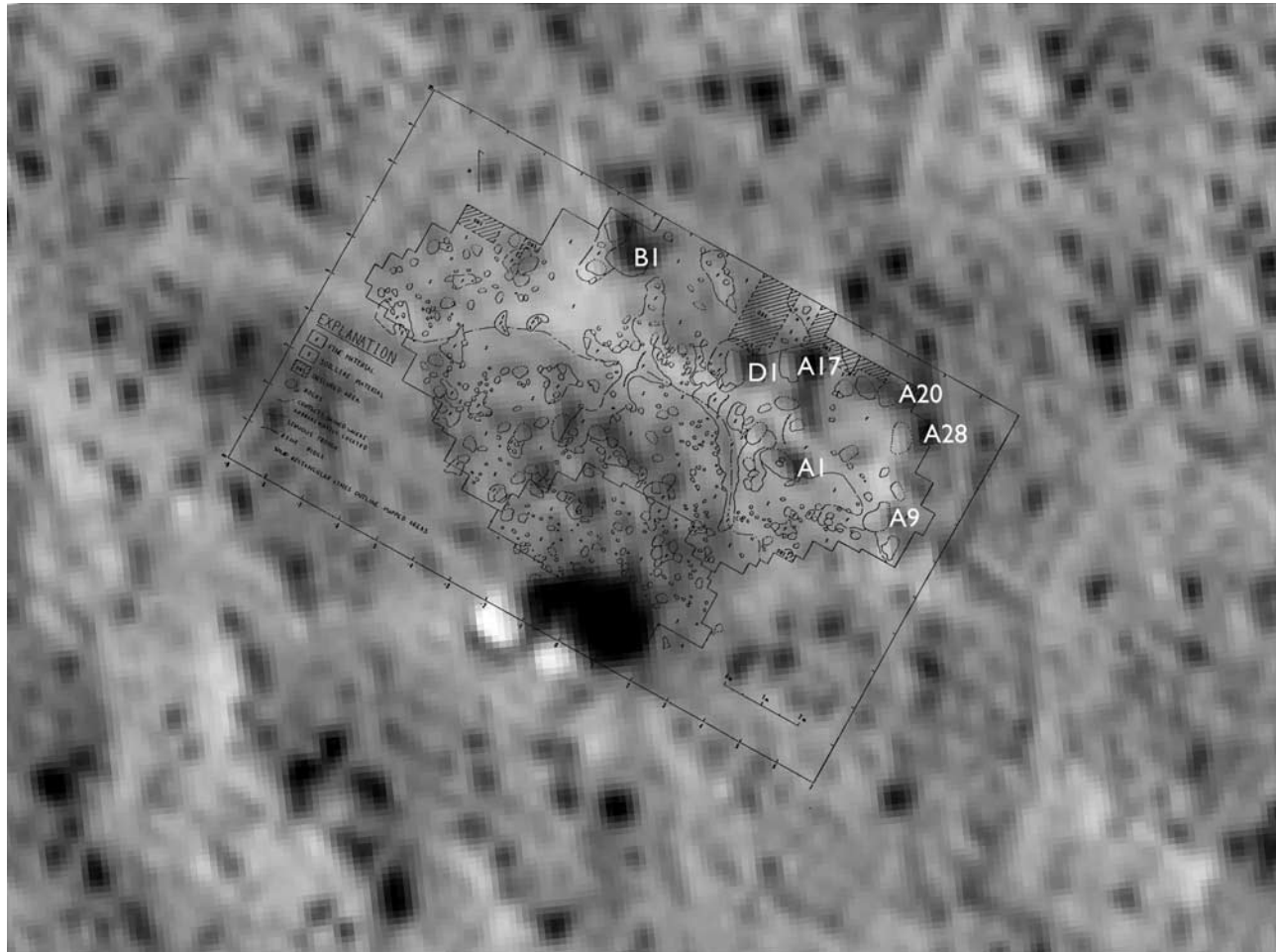
Figure 25. Close-up of VL2 in HiRISE with surface map from lander images [*Moore and Keller*, 1991] superimposed. The seven largest rocks in Figure 24 are labeled (from left to right in the map: B1, D1, A1, A17, A9, A20, and A28) and correspond exactly with shadows cast in the HiRISE image. Surface map shows rocks and soils in 16 m by 10 m area with "near field" marked within ~3 m and the "far field" beyond (tick marks along edge of the map are 1 m apart). Image is "super resolution" composite of three HiRISE images of the VL2 site (PSP_001501 2280_RED, PSP_001976 2280_RED, PSP_002055 2280_RED). Images are scaled and oriented so that objects around the lander can be registered at subpixel scales (1/5th), then averaged together at 200% the original size. The result is a reduced alias image of the lander surroundings, making small features somewhat easier to compare with the Viking ground views.
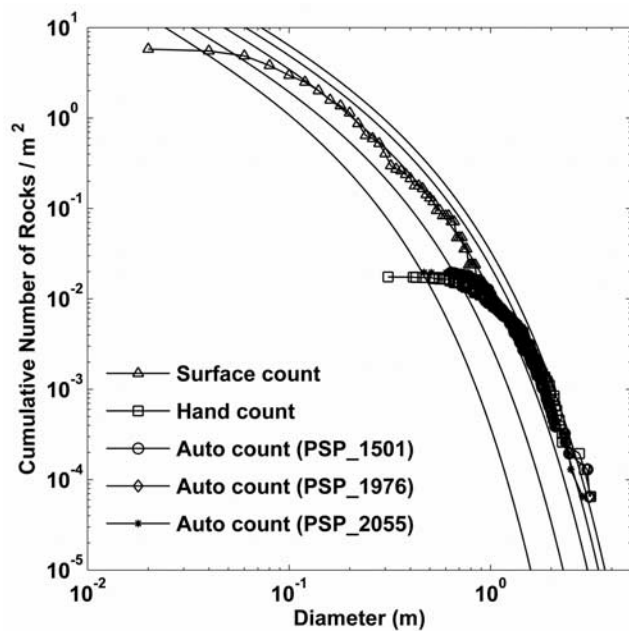
Figure 26. Plot of the cumulative number of rocks larger than a given diameter per meter squared versus diameter for rocks counted in three HiRISE images using the rock detector software and a hand count and from the VL2 lander (surface) [*Moore and Keller*, 1991]. Curves are model distributions for 5%, 10%, 20%, 30%, and 40% cumulative fractional area. Note roll-off in HiRISE measurements relative to the model for diameters less than $1-2$ m and continuity with measurements from the lander indicating that the roll-off is a resolution effect and that the actual rock distribution extend from meter to centimeter diameter roughly parallel to the model distributions. HiRISE images 1501, 1976, and 2055 at 0.31 m/pixel had 300, 281, and 302 rocks, respectively over 24,025 m^2 areas centered on VL2.

about 1.5 m in diameter (Figure 28). This rock clearly shows up in the HiRISE image just to the northeast of the lander and is among the larger rocks visible in the image.

[30] Automated rock counts of 2 HiRISE images of similar $\sim 70,000$ m^2 areas around VL1 are shown in Figure 29. The cumulative number of rocks larger than a given diameter per meter squared versus diameter of both counts parallels the exponential model curves for $8-10\%$ cumulative fractional rock coverage and vary from 10^{-5} to 4×10^{-4} rocks/m^2 for diameters between 1.2 and 2 m, but rolls off to lesser rock coverage below 1.1 m diameter. Rock counts from the ~ 84 m^2 area of the "near and far field" of VL1 (not including outcrop [*Moore and Keller*, 1990]) also parallel the model curves for $8-10\%$ rock coverage but with more than an order of magnitude more rocks (10^{-2} to 5 rocks/m^2) for rock diameters of 5 to 50 cm. So even though the rock counts from the lander and from HiRISE images are not continuous, they fall on the same model distribution for $8-10\%$ rock coverage, indicating that both lander and orbiter are seeing the same rock population.

[31] Rocks visible in HiRISE images south of the lander and in other areas in the general vicinity of VL1 show much higher concentrations of boulders associated with rims and

ejecta deposits of moderately degraded impact craters. Similar higher concentrations were estimated in distant portions of the VL1 lander panoramas. Specifically, *Golombek and Rapp* [1997] estimated the size and distance to the largest 17 rocks (>0.8 m diameter) out to 80 m from the lander in the southeast direction, which includes the rim of a 150-m-diameter partially degraded crater. The rock size-frequency distributions of the entire 20,000 m^2 area surveyed and the smaller 2000 m^2 crater rim (C) are elevated relative to the background plains and generally parallel exponential model distributions for 20% and 30% rock coverage, respectively [see *Golombek and Rapp*, 1997, Figures 3, 6, and 8]. The slightly rockier southern area of Figure 27 was tabulated separately, and the rocky rim of crater C was also counted in the HiRISE image. Results show remarkable agreement with surface estimates with the southern portion of the image having rock distributions that parallel the model for about 20% rock coverage for diameters between 2 and 3 m. The crater rim has rock distributions that parallel the model for 30% rock coverage for diameters between 1.7 and 2.2 m. As a result, similar variations in rock density are recorded in both HiRISE and lander images over greater areas and distances from the lander.

6.4. Mars Pathfinder

[32] Mars Pathfinder was the third lander imaged by HiRISE and is located on a rougher and rockier surface than either of the Viking landers (Figure 30). The HiRISE image clearly distinguishes the lander and the deployed ramps (to the southwest) used to drive the rover off the lander. The largest rock within 10 m of the lander (Figure 31), Yogi (1.2 m diameter) is clearly visible about 5 m north of the lander in the HiRISE image (Figure 30).

[33] An automated rock count was done around the lander in HiRISE image PSP_001891_1995. The cumulative number of rocks larger than a given diameter per meter squared versus diameter in the HiRISE image parallels the exponential model curves for $10-20\%$ cumulative fractional rock coverage and varies from 10^{-4} to 10^{-5} rocks/m^2 for diameters between 1.5 and 3 m, but rolls off to lesser rock coverage below 1.5 m diameter (Figure 32). Also shown are the 4430 rocks counted within a 186 m^2 area within around 20 m of the lander reported by *Golombek et al.* [2003]. Rock distribution varies from 7 to 40% rock coverage around the annulus but averages 19%. The size-frequency distribution of the rocks viewed from Pathfinder shown in Figure 32 parallels the model curves for about 12% rock coverage for rock diameters of $0.4-0.7$ m and parallels the model curve for $\sim 20\%$ rock coverage for smaller and larger diameters. The behavior of the size-frequency distribution in the HiRISE counts is similar with some portions of the distribution paralleling the 12% model curve and other portions closer to the model for 20% rock coverage. Counts in slightly different portions of the HiRISE image also show a similar behavior with the portions of the cumulative number of rock distribution parallel to the exponential model curves for 20% rock coverage at around 3 m diameter as indicated by the largest rock in Figure 32. Thus, as for VL1 and VL2 landers, rock distributions in HiRISE images at greater than 1.5 m diameter can be extrapolated along model curves to smaller diameters where they are parallel to model curves for similar rock coverage. This indicates that
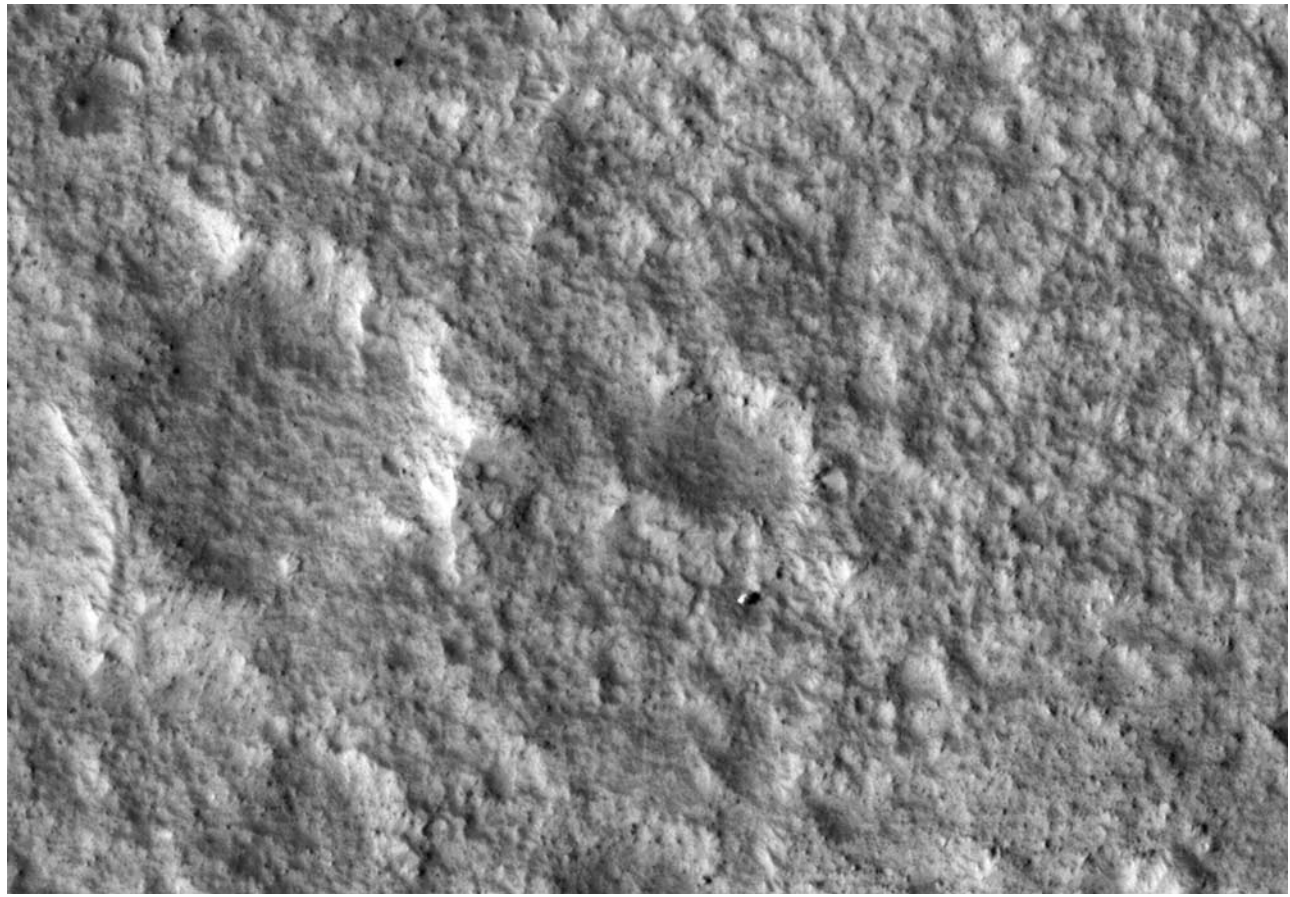
Figure 27. HiRISE image of Viking Lander 1 (largest object in lower central portion of image). PSP 001719-2025 image is 0.29 m/pixel 226 m by 157 m with north up and solar elevation of 40°. Note much less rocky plain than VL2 with the largest nearby rock, Big Joe (1.5 m diameter), about 10 m to the northeast.

HiRISE is seeing the same population of rocks seen in lander images at all three rocky landing sites. Further, because the size-frequency distributions parallel the same model curves based on lander rock distributions for the total rock coverage, the model distributions can be applied to larger diameters (and larger areas). These results indicate the size-frequency distributions can be reliably extrapolated along model curves to estimate the number of rocks at diameters smaller than can be resolved by HiRISE.

7. Phoenix Landing Site Rock Size-Frequency Distributions and Hazards

7.1. Landing Site Rock Distributions

[34] Because regions A, B, and C selected for landing Phoenix prior to the return of HiRISE images all have dense boulder fields associated with degraded craters throughout, landing ellipses for Phoenix could not be safely placed to avoid them. As a result, thermal images were used to find areas with fewer boulder fields. The location selected after extensive imaging by HiRISE is in region D, just west of region A, with the landing ellipse placed in a relatively rock-free valley at 68.16°N latitude, 233.35°E longitude [*Arvidson et al.*, 2008]. Figure 33a shows a representative HiRISE image (PSP_001893_2485) just west of the center

of the ellipse. Figure 33b shows the map of areas covered by 0–1 (blue), 2–3 (green), 4–8 (yellow), 9–19 (orange), and >20 (red) rocks per hectare greater than 1.5 m in diameter generated by the rock detector. This map is slightly different than the map in Figure 19 in that the number of rocks is keyed to 1.5 m diameter rocks (rather than all rocks), because that is the average diameter at which the HiRISE measured distributions fall beneath the model and makes for a more accurate extrapolation to smaller diameters. Figure 33a also shows the locations of examples of areas for the five different rock density areas that are shown in Figure 34. The size-frequency distribution of rocks in each of the five areas in shown in Figure 35. The cumulative number distributions have 1, 2, 4, 19, and 30 rocks greater than 1.5 m diameter and correspond to exponential model curves of ∼7%, ∼8%, ∼14%, ∼19%, and ∼30% total rock coverage. The behavior of the rock distributions is similar to other areas of the northern plains with the maximum rock size and rollover diameter increasing with increasing rock density.

7.2. Extrapolations to Potentially Hazardous Diameters

[35] The observation that areas with low, medium, and high rock densities in the landing ellipse and throughout the
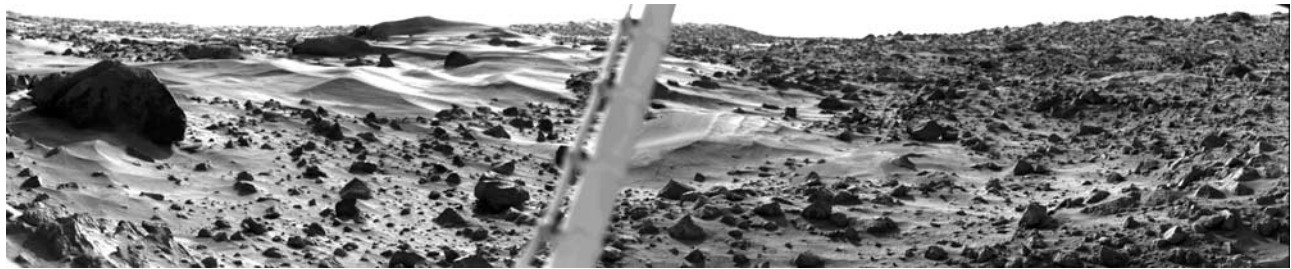
Figure 28. VL1 image of surface toward the east showing Big Joe (left) and light toned drift deposits. Big Joe, the largest, closest rock to VL1 is about 10 m away and 1.5 m in diameter. Whale, a 2 m diameter rock is about 25 m away from the lander near the horizon to the right of Big Joe but cannot be seen in the HiRISE image likely because of the cover of light drift (which does show up in the HiRISE image).

northern plains of Mars have rock size-frequency distributions that parallel exponential model rock distributions for rocks >1.5 m in diameter allows the use of the model to extrapolate to the cumulative fractional area covered or the cumulative number of rocks larger than any diameter of interest. Using the rock distributions within the ellipse as a guide, calculations will be performed for very low, low, medium-low, medium-high, and high rock densities that correspond to $0-1$, $2-3$, $4-8$, $9-19$, and >20 cumulative number of rocks greater than 1.5 m in diameter per square hectare, which fall along exponential model total rock coverages of ~5%, < 10%, < 15%, < 20%, and >21%. The cumulative number of rocks larger than three diameters of interest are shown in Table 3 that correspond to extrapolations along the model curves for the total rock coverage where it intersects the equivalent cumulative number of rocks larger than 1.5 m diameter.

[36] The Phoenix lander is sensitive to rocks higher than the leg height during touchdown and to rocks higher than the two fan like solar arrays that open after landing. The legs of the Phoenix lander provide about 45 cm of clearance when accommodating an average amount of leg crush during touchdown. Accommodating higher remaining velocities at touchdown produces more leg crush and reduces clearance to about 33 cm. The area of the base of the lander and propulsion tanks is estimated to be 1.755 m^2. Because rocks on Mars from lander and HiRISE measurements have diameters that average about twice their height, rocks that are 0.9 m and 0.7 m in diameter are considered as being potentially hazardous if encountered during touchdown of the Phoenix lander. Two 1 m radius fan shaped solar arrays extend out from either side of the lander after landing to provide solar power for operations. The arrays open on arms and basal support structures that are about 51 cm above the ground and sweep out a combined area of about 6 m^2. As a result, rocks higher than 0.6 m high (~1.2 m diameter) could prevent full solar array deployment thereby substantially reducing power for operations. These are the three diameters for which cumulative number of rocks are provided for different rock density areas in Table 3.

7.3. Probabilities of Encountering Potentially Hazardous Rocks

[37] Using the estimated cumulative number of rocks, the probability that one rock larger than the appropriate size will be present over an area of the lander base or solar arrays is calculated for a Poisson distribution of rocks most appropriate to the observed long-tailed rock distributions and the natural processes that produced them [*Haight*, 1967].
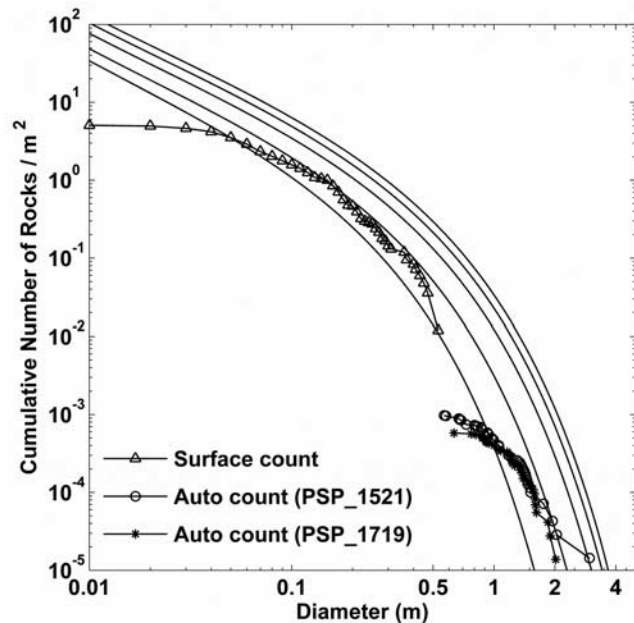

Figure 29. Plot of the cumulative number of rocks larger than a given diameter per meter squared versus diameter for rocks counted in two HiRISE images and from VL1 (surface) [*Moore and Keller*, 1990]. Curves are model distributions for 5% to 40% cumulative fractional area (lines from left to right). Note roll-off in HiRISE measurements relative to the model for diameters less than 1.5 m and continuity with measurements from the lander indicating that the roll-off is a resolution effect and that the actual rock distributions extend from meter to centimeter diameter roughly parallel to the model distributions. HiRISE images PSP_1521_2025 and PSP_1719_2025 are 0.30 and 0.29 m/pixel with solar elevations of 40° and 21°, respectively. Sixty-nine rocks counted in 288 m by 242 m (69,775 m^2) area in HiRISE image PSP_1521_2025 and 43 rocks counted in 301 m by 241 m (72,494 m^2) area in PSP_1719_2025.

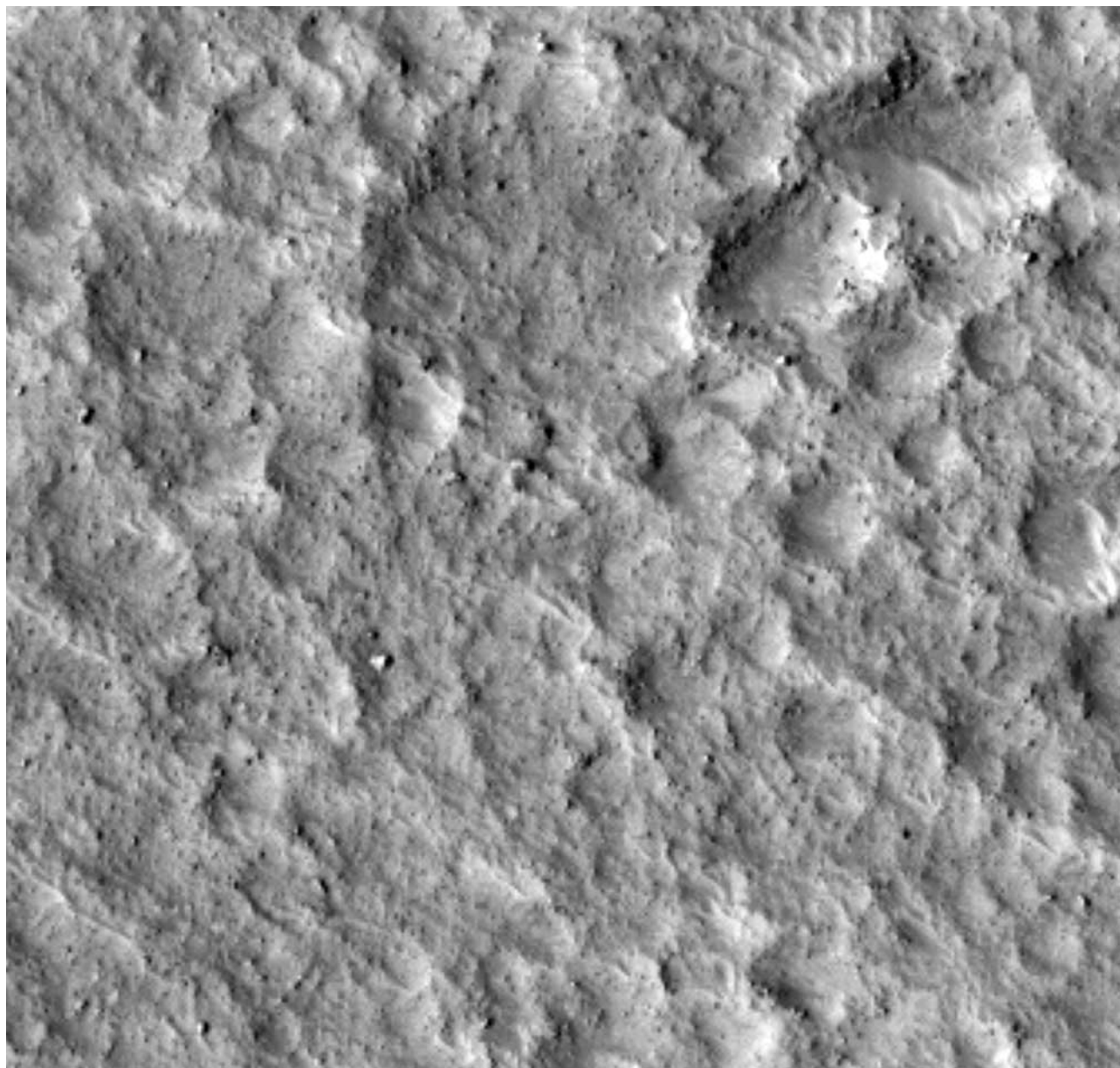**Figure 30.** HiRISE image of MPF and surrounding rocky plain. The largest rock, Yogi is about 5 m north from the lander and is 1.2 m in diameter. The rock Couch that can be seen from the lander on the horizon in Figure 31 is the large oblong rock on the edge of the image toward the northwest. Area shown is 188 m by 179 m of HiRISE image PSP_1890_1995 is 0.28 m/pixel with a solar elevation of 37.5°.

Figure 31. Mars Pathfinder image of Sojourner rover measuring the composition of largest nearby rock Yogi, which is 5 m away and 1.2 m in diameter. Rocky plain with many large rocks are evident in HiRISE image shown in Figure 30, including Couch on the left horizon.

Details on the method and calculation are presented by *Golombek et al.* [2003], and the results for 1.2 m diameter rocks that could impede opening of the solar arrays and 0.9 and 0.7 m diameter rocks that the lander base could encounter during landing are provided in Table 4. The probability the lander would encounter one rock higher than its base when landing for average leg crush is <1% for areas with low (<10%) rock abundance. Because most of the valley selected for landing Phoenix is composed of similar low rock abundance surfaces [*Arvidson et al.*, 2008], the Phoenix lander has a high probability of landing with average leg crush without encountering large potentially hazardous rocks. Medium rock abundance surfaces have higher probabilities (1.9–3.4%) of encountering potentially hazardous rocks (>0.9 m diameter) and high rock abundance areas have even higher probabilities. These probability calculations are similar to extensive Monte Carlo simulation results carried out by the Phoenix project for landing site certification. The probabilities of encountering rocks higher than 0.35 m (assuming more leg crush during landing) increases from 0.5 to 2.8% for low rock abundance surfaces to 5–8% for medium rock abundance surfaces to >10% for high rock abundance surfaces. The lander solar arrays also have a low probability (<1%) of encountering a rock higher than 0.6 m that might impede their deployment in low rock abundance surfaces. These probabilities increase to ∼3% for medium rock abundance surfaces and >5% for high rock abundance surfaces. Rock detector mapping of all HiRISE images in the selected landing ellipse show that most of the surface in the ellipse has 0–3 rocks >1.5 m in diameter, which corresponds to low rock abundances and thus has less than a 1% chance of encoun-tering a potentially hazardous rock during landing or a rock that could impede the opening of the solar arrays.

8. Proximity of Rocks During Phoenix Operations

8.1. Introduction

[38] Although large rocks are potential hazards during landing and opening of the solar arrays, the presence of smaller rocks after landing in the robotic arm workspace could be beneficial to the mission. An important science objective of the Phoenix lander is to analyze the composition and chemistry of the soil overlying the ground ice [*Smith et al.*, 2008], and as a result, the thickness of this overlying soil was a factor in site selection [e.g., *Arvidson et al.*, 2008]. However, there is concern that the descent engines could possibly blow away overlying soil during landing [e.g., *Plemmons et al.*, 2008], which is estimated to be only several centimeters thick at the selected landing site [e.g., *Arvidson et al.*, 2008; *Mellon et al.*, 2008]. Detailed thermal modeling by *Sizemore and Mellon* [2006] shows that rocks 0.05 to 1 m in diameter that protrude from the surface would maintain an ice free zone comparable to the dimension of the rock. As a result, rocks of this size range would have ice free soil around them that would be less likely to erode by the thrusters during landing. In addition, rocks of this size would have ice free soil beneath them, which would provide soil at greater depths for examining possible gradients in soil texture or chemistry with depth and possible gradients in thermal environment that could affect soil moisture and the presence of potential habitats and/or the deposition and accumulation of salts.

[39] Rocks in the 2–7 cm diameter size range are small enough to fit within the scoop at the end of the robotic arm
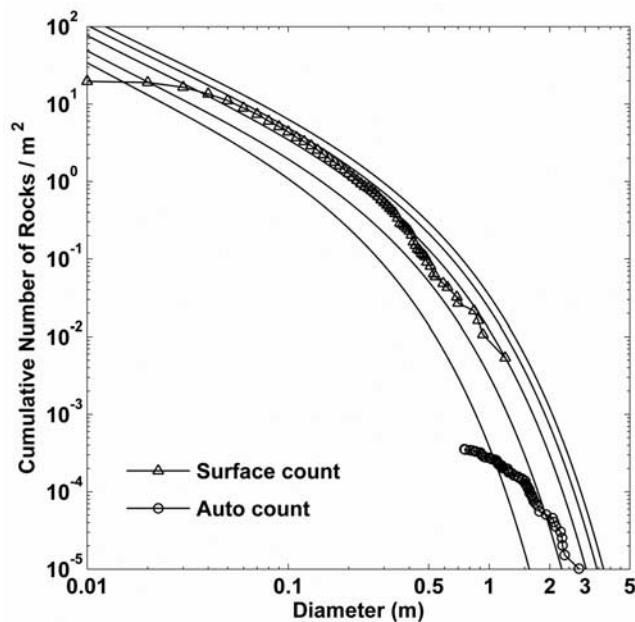
Figure 32. Plot of the cumulative number of rocks larger than a given diameter per meter squared versus diameter for rocks counted in two HiRISE images and from MPF (surface) [*Golombek et al.*, 2003]. Curves are model distributions for 5% to 40% cumulative fractional area (from left to right). Note roll-off in HiRISE measurements relative to the model for diameters less than 1−1.5 m and continuity with measurements from the lander indicating that the roll-off is a resolution effect and that the actual rock distributions extend from meter to centimeter diameter roughly parallel to the model distributions. Seventy-two rocks were counted in 375 m by 525 m area in PSP_1890_1995.

and can be picked up [*Bonitz et al.*, 2008]. Picking up small rocks offers the prospect of examining rock texture, morphology and color to help identify mineralogy and rock type more closely at higher resolution with the Surface Stereo Imager and the Robotic Arm Camera. Rocks of this size and up to 10 cm in diameter can also be pushed on the surface, allowing the inspection of the rock underside to look for variations in surface weathering and to investigate the soil beneath the rock as described above. All rocks with diameters from 2 cm to 1 m will be an asset to direct investigation of soils, because the ice table is expected to be deeper than average in the region of a rock's thermal influence. Larger rocks, 10s of cm to 1 m, will not be movable by the scoop, but should be associated with laterally extended regions of relatively deep ice-free soil. In addition to providing materials for soil investigations and protecting the soil from thrusters during landing, rocks will provide opportunities for testing current theoretical models of ground ice stability. Moving small rocks and measuring the thickness of the ice free soil around larger rocks will allow for direct comparison to simulations of the thermal response of ground ice to soil heterogeneities [e.g., *Sizemore and Mellon*, 2006]. This type of detailed comparison can be used to better understand ground ice stability in the current climate and dynamical response to climate change. In this

section, model rock size frequency distributions representative of the distributions measured in HiRISE images are extrapolated to smaller diameter as a means of estimating the number of rocks in these size ranges that are likely to be present within the robotic arm workspace.

8.2. Method

[40] To estimate the number of small diameter rocks at the Phoenix landing site, representative size-frequency distributions measured in HiRISE images of the landing ellipse were extrapolated along exponential model curves. In general, areas within the landing ellipse have very low rock abundance with rock counts in HiRISE images that correspond to model distributions around 1−5% cumulative fractional area coverage. Other surfaces in the vicinity of the landing ellipse have small areas with rock counts in HiRISE images that correspond to model distributions of around 10%, 20% and >20% cumulative fractional area coverage. On the basis of these observations, first the model cumulative number of rocks greater than diameter 2, 5, 7, 10, 25, 50 and 100 cm per m^2 was calculated by numerically integrating the exponential cumulative fractional area distributions determined using equation (1) (see section 1). Next, to determine the number of rocks per m^2 within any given diameter interval, the cumulative number of rocks greater than the maximum diameter per m^2 was subtracted from the cumulative number of rocks greater than the minimum diameter per m^2. This number was multiplied by the robotic arm workspace area, estimated to be a 1.95 rad sector annulus from 0.6 m to 2.07 m distance, which is 1.07 m from the lander deck and measures about 3.8 m^2 [*Bonitz et al.*, 2008]. The number of rocks of 5−100 cm, 7−100 cm, 10−100 cm, 2−7 cm, 5−7 cm and 5−10 cm diameter intervals expected within reach of the arm is shown in Table 5 for 1%, 3%, 5%, 10%, 20%, 30% and 40% cumulative fractional area rock coverage.

[41] The first 3 diameter intervals correspond to rocks that could produce depressions in the ice layer thickness that would be helpful for sampling dry layer material [e.g., *Sizemore and Mellon*, 2006]. Because rocks larger than 5 to 10 cm are estimated to produce a layer of dry soil around them, the number of rocks greater than 5 cm, 7 cm, and 10 cm but smaller than 1 m are estimated. The next 2 diameter intervals are the number of rocks small enough to be picked up by the scoop. The arm is capable of picking up pebbles 2−7 cm in diameter, but because of uncertainties in the number of small pebbles in the 2 cm to 5 cm diameter range, estimates were provided for the number of pebbles larger than each, but smaller than 7 cm.

[42] Rock counts from existing landing sites with more dust and eolian deposits (fines) have fewer small pebbles compared to the model than less dusty landing sites (fines can easily mask small pebbles) [*Golombek et al.*, 2008]. For example, at the VL1 and VL2 landing sites, which have lower thermal inertia and more dust and eolian deposits than the other rocky landing sites, rock size-frequency distributions roll-off below the model distributions at diameters <10 cm [*Golombek et al.*, 2006, 2008]. In contrast, the MPF landing site, which has a higher thermal inertia and fewer fines, has many more pebbles and the rock size-frequency distribution does not fall below the model until smaller diameters. The same relationship is found in counts of rocks
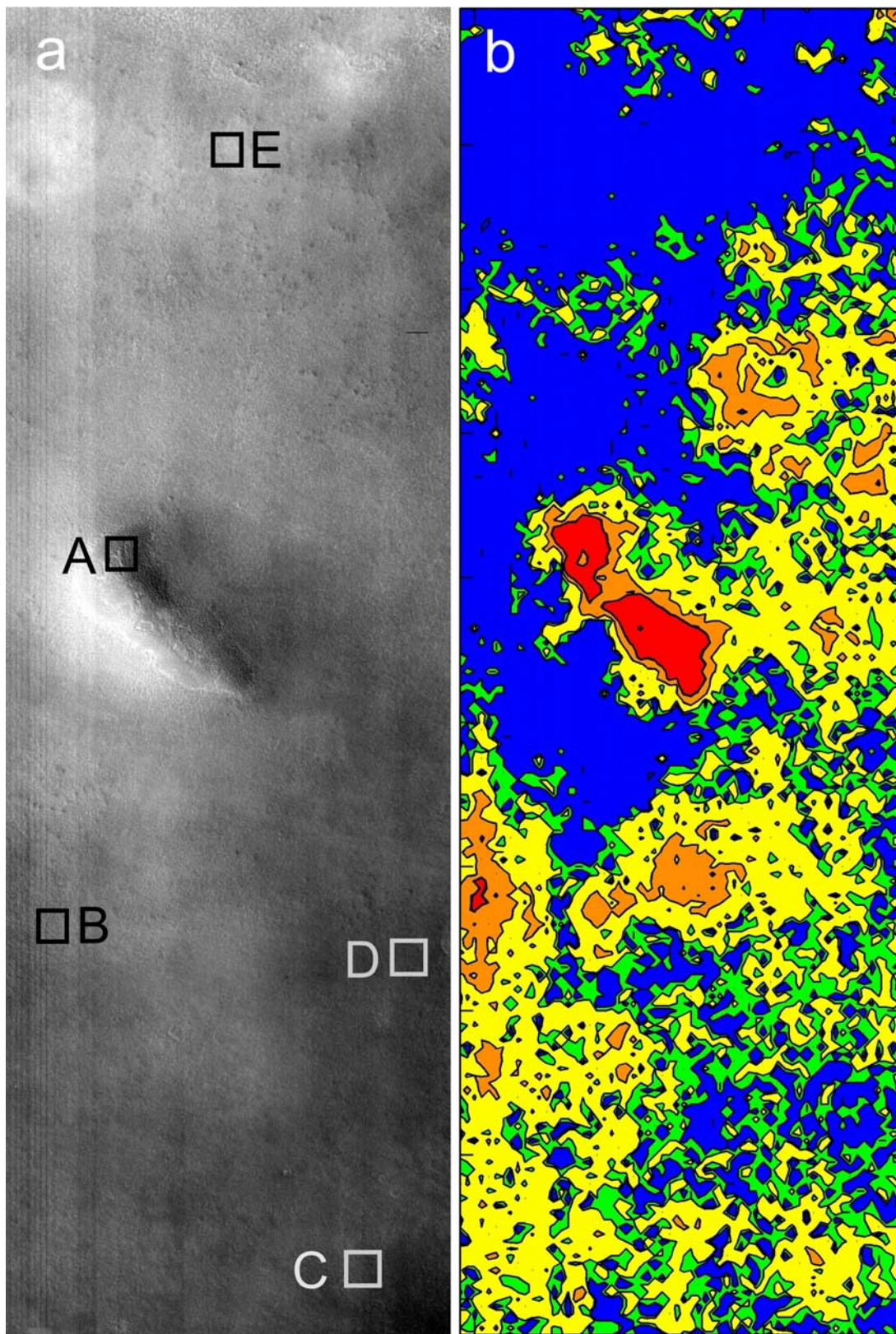
Figure 33. (a) HiRISE image PSP_001893_2485 (0.31 m/pixel) of a portion of the landing site selected for Phoenix showing plain with relatively few rocks. Image is 6.2 km wide. Areas (squares with 186 m sides) shown are illustrated in Figure 34. North is up. (b) Thematic map of 0–1 (blue), 2–3 (green), 4–8 (yellow), 9–19 (orange), and >20 (red) rocks greater than 1.5 m in diameter per square hectare derived from the rock detector software of HiRISE image PSP 001893-2485 shown in Figure 33a. Ticks at edge of image are ∼2 km apart.
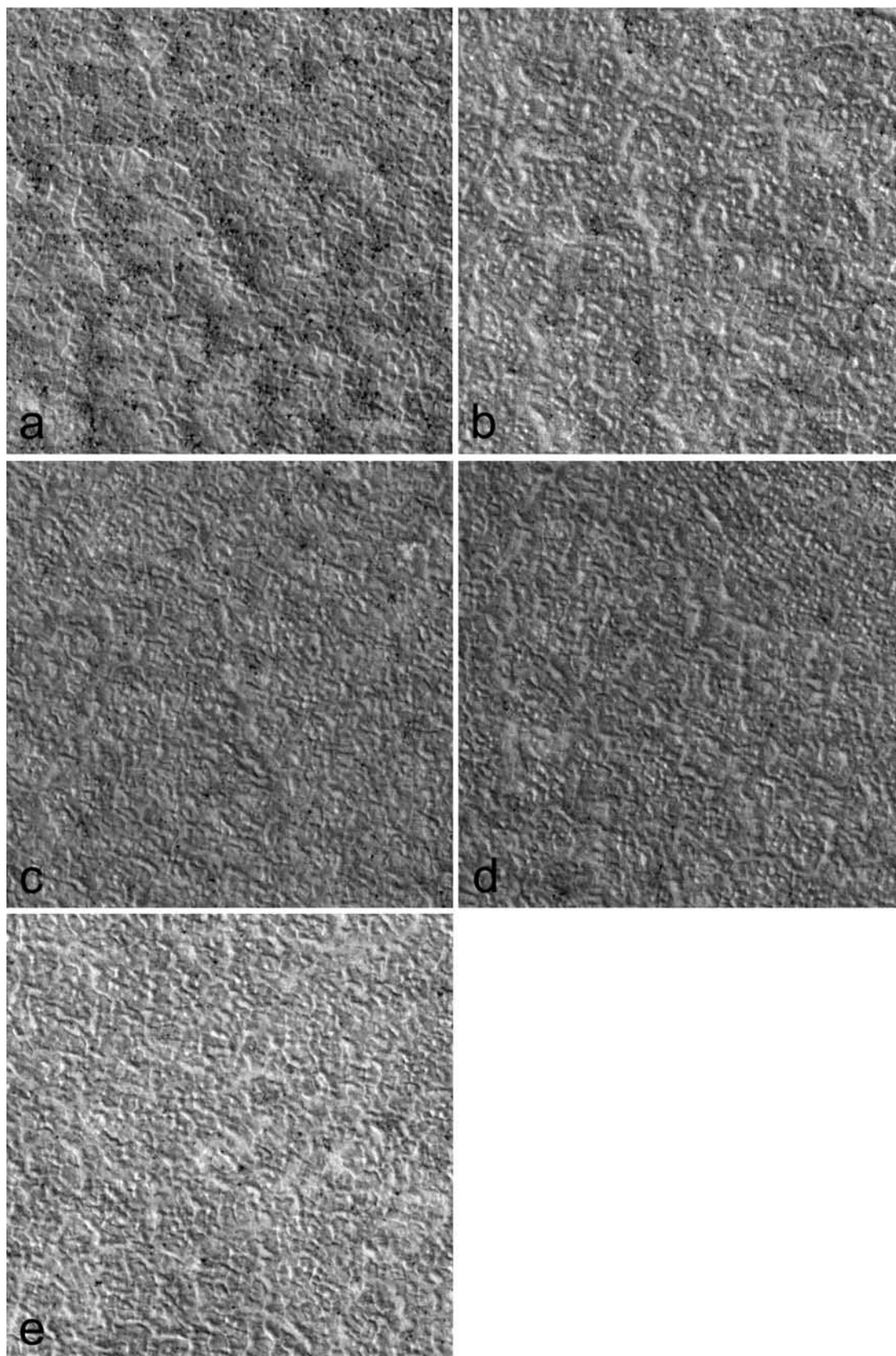
Figure 34

Figure 35. Cumulative number of rocks larger than a given diameter per m^2 versus diameter of five areas shown in Figure 34 (locations of these areas are shown in Figure 33a and colors refer to rock densities mapped in Figure 33b). Also shown from left to right are model curves for cumulative fractional area rock coverage of 5%, 10%, 20%, 30%, and 40%, respectively. Rock dis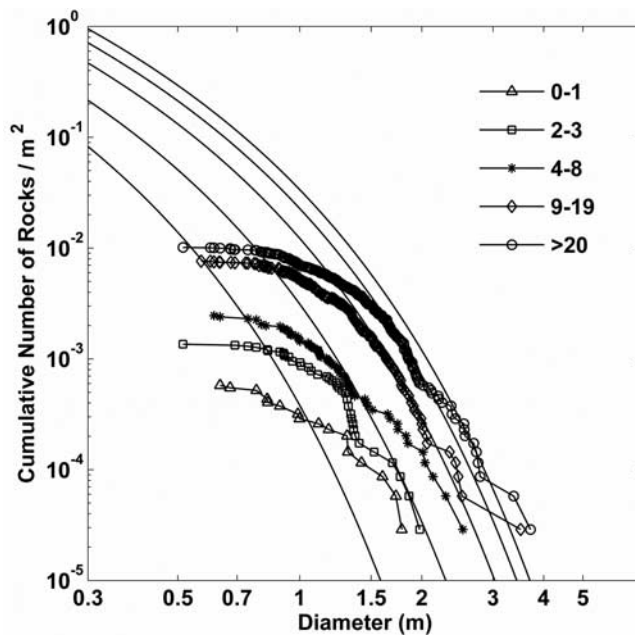tribution for red area with >20 rocks greater than 1.5 m in diameter per square hectare is parallel to the model distribution for 30–40% fractional area rock coverage. Rock distributions for blue, green, yellow and orange, corresponding to <1, 2–3, 4–8, and 9–19 rocks greater than 1.5 m in diameter per square hectare are parallel to the model distributions for 5–8%, 8–10%, 15–17%, and 20% fractional area rock coverage, respectively.

and pebbles in the cratered plains of Gusev, where rock distributions in low-albedo, less dusty portions of the plains match the model distributions down to 2 cm diameter, and rock distributions in higher albedo, dustier portions of the plains fall below the model distributions at diameters <4 cm [*Golombek et al.*, 2006]. These examples indicate that deposition of eolian deposits and atmospheric dust can reduce the number of pebbles found at the surface. The albedo (a proxy for dustiness of the surface [*Golombek et al.*, 2005, 2008]) of the Phoenix landing site is moderate and comparable to portions of the Gusev cratered plains and the Mars Pathfinder landing site, both of which have a large population of pebbles comparable to the model distributions. As a result, to first order there is no reason to expect that the Phoenix landing site would not have plenty of

pebbles in the 2–5 cm size range. The final interval of rocks (0.05–0.1 m diameter) are those that could to be pushed by the arm, providing the opportunity to explore dry material under rocks.

[43] It should be noted that this method assumes that the model distributions apply and those measured in HiRISE images can be extrapolated to small diameter as argued by the rock size-frequency distributions from the surface following the expected model distribution for diameters larger than about 10 cm [*Golombek et al.*, 1999, 2005]. The distribution of rocks on the surface is also assumed to be homogeneous for any given total rock coverage. Processes that could sort or process rocks, such as periglacial processes suggested by the ubiquitous polygons, would obviously alter the spatial distribution of rocks. Thermal contraction polygons are known to process rocks on the surface, creating rubble piles or concentrating rocks along polygon edges, both of which are observed in HiRISE images of the northern plains. Nevertheless, the exponential model distribution is based on basic fracture and fragmentation theory that has been applied successfully to a broad variety of surfaces on the Earth and terrestrial planets, which suggests that the basic population of rocks is likely similar due to the similar production process, but that periglacial processes have simply spatially sorted the populations in the northern plains [e.g., *Mellon et al.*, 2008]. In any case, this is a hypothesis that can be tested using the model extrapolations, and results provide a quantitative estimate of what can be expected for use in planning operations.

8.3. Results

[44] Results are encouraging in that there should be rocks within the robotic arm workspace even for fairly rock free areas in the targeted Phoenix landing site. For areas with only 1% rock coverage, at least 1 rock 0.07–1 m diameter should be in the area that can be reached by the arm. Areas with higher rock coverage (3%, 5% and 10%) should have more rocks (5, 7, and 12, respectively). High rock abundance areas (>20%) that are generally being avoided for landing Phoenix, but for which some small areas cannot be avoided in the ellipse, should have even more rocks 0.07–1 m in diameter (22–40 rocks for 20–40% rock coverage). These calculations suggest that even for very low rock abundance areas within the ellipse, rocks large enough to create a surrounding ice free soil layer large enough to be sampled by the robotic arm should be present, thereby partially ameliorating concerns of the descent engines blowing away all surface soil.

[45] Extrapolations to rock diameters small enough to be picked up by the robotic arm (2–7 cm diameter) suggest that multiple rocks should be present for investigation even in very low rock abundance areas. Assuming 2–7 cm pebble distributions are similar to the model, results suggest

Figure 34. Areas (186 m across, covering 34,596 m^2) shown in 33a from HiRISE image PSP_001893_2485 (0.31 m/pixel) (colors refer to rock densities mapped in Figure 33b). (a) Surface A (red) with >20 rocks greater than 1.5 m in diameter per square hectare; 351 rocks counted. (b) Surface B (orange) with 9–19 rocks greater than 1.5 m in diameter per square hectare; 284 rocks counted. (c) Surface C (yellow) with 4–8 rocks greater than 1.5 m in diameter per square hectare; 85 rocks counted. (d) Surface D (green) with 2–3 rocks greater than 1.5 m in diameter per square hectare; 45 rocks counted. (e) Surface E (blue) with 0–1 rocks greater than 1.5 m in diameter per square hectare; 21 rocks were counted.

Table 3. Cumulative Number of Rocks Larger Than Four Diameters for Different Rock Density Areas and the Equivalent Model Total Rock Coverage

Rock Density	Model Total Rock Coverage (%)	Cumulative Number of Rocks With Diameter			
		>1.5 m per Square Hectare	>1.2 m per Square Meter	>0.9 m per Square Meter	>0.7 m per Square Meter
High	30	37	0.01	0.035	0.08
	>21	>20			
Medium high	<20	9–19	0.005	0.02	0.05
Medium low	<15	4–8	0.0025	0.011	0.03
Low	<10	2–3	0.001	0.001	0.003
Very low	~5	0–1	0.00009	<0.001	<0.003

that 20–60 rocks of this size range are expected to be present in areas of 1–10% rock coverage (Table 5). Areas with total rock coverage of 20–40% are expected to have 95–164 rocks of 2–7 cm diameter available for manipulation with the robotic arm and scoop. If Phoenix lands in areas that have fewer pebbles in the 2–5 cm diameter range than suggested by the extrapolations, but similar to dustier landing sites, there still should be 2–8 rocks of 5–7 cm diameter available in the robotic arm workspace for investigation.

[46] Rocks large enough to create an ice free soil zone surrounding them, but small enough to be pushed by the robotic arm are also expected to be present. For areas with total rock coverage of 1–10%, 3–14 rocks 5–10 cm in diameter are expected to be present within reach of the robotic arm (Table 5). For areas with total rock coverage of 20–40%, 22–39 rocks 5–10 cm in diameter are expected to be present. These results suggest that the Phoenix mission will have the opportunity to investigate ice free soils beneath rocks at levels below the expected average ice table depth.

9. Summary

[47] Prior to Mars Reconnaissance Orbiter (MRO) arriving at Mars, dark pixels tentatively identified as boulders in MOC images were counted to help with selection of a Phoenix landing site within three broad regions (A, B, and C) of the northern plains. Narrow angle MOC images (~3 m/pixel) of the northern plains show low-albedo clusters composed of dark pixels typically located around numerous degraded or pedestal craters in the northern plains. In one higher resolution MOC image (~0.5 m/pixel), the dark pixels appear to be shadows behind boulders in the direction of solar illumination. Counts of these dark pixels showed the fields covered only 5.6% of the area in MOC images and that the dark pixels themselves covered only ~1% of the surface area. Size-frequency distributions of the dark pixels show similar slopes to lander distributions and exponential models derived from them, but they are displaced to larger diameters and so are difficult to relate to typical rock distributions.

[48] Higher resolution HiRISE images clearly resolve individual rocks in the boulder fields with bright sunlit sides and shadows, and show that the dark pixels in MOC images are mostly shadows of clusters of smaller rocks. HiRISE images of prospective locations in regions A, B, and C and throughout most of the northern plains show that dense rock fields associated with degraded impact craters are ubiquitous, and that Phoenix landing ellipses cannot be located to avoid them. These regions were abandoned for landing Phoenix, and thermal images were used to locate areas with fewer rocks.

[49] An automatic rock detection algorithm was adapted and used to count more than 10 million rocks larger than 1 m in diameter and map the rock distributions in >1500 km^2 area during the Phoenix site selection process. The rock detector employs a modified maximum entropy thresholding technique using a nonlinear image stretching routine that segments shadows cast by rocks from nonshadowed pixels. The software then fits an ellipse to the shadow and a cylinder to the rock to derive the rock diameter and height (from the shadow length). Tests of the performance of the detector on spacecraft of known size on the surface of Mars shows the algorithm accurately determined spacecraft diameter and height to within 1–2 pixels, which is about the limit of what could be expected.

[50] Measurement of rock distributions for rocks >1.5 m diameter throughout the northern plains in HiRISE images parallel model distributions derived from lander rock counts of smaller diameter. Rock distributions at large rock diameter parallel models for cumulative fractional area covered by 5% to 90% rocks, where the greatest density of rocks in fields around craters have 30–90% rock coverage, less dense fields around craters have 10–30% rock coverage, and background terrain away from craters have 0–10% rock coverage. At rock diameters between 1 and 2 m, HiRISE distributions flatten considerably well below lander rock distributions or the exponential models derived from them and appear to be influenced by image resolution, which makes it difficult to recognize all objects less than about 5 pixels across.

[51] Comparison of rock distributions around Viking Lander 1, 2 and Mars Pathfinder show that above around 1.5 m diameter HiRISE counts are parallel to the same model rock distribution (10–20%) as measured from the ground for rocks <1 m diameter, and that the same large

Table 4. Probability of Encountering One Rock Higher Than the Solar Array Supports During Deployment and Higher Than the Lander Base During Landing for Two Cases of Leg Crush

Rock Density	Model Total Rock Coverage (%)	Probability Array Encounters Rock Diameter (%)		
		>1.2 m	>0.9 m	>0.7 m
High	30	5.82	5.96	13.1
	>21			
Medium high	<20	2.95	3.45	8.4
Medium low	<15	1.49	1.91	5.13
Low	<10	0.60	0.87	2.77
Very low	~5	0.05	0.17	0.52

Table 5. Model Number of Rocks in the Indicated Rock Diameter Interval Expected Within the 3.8 m² Area That the Phoenix Arm Can Reach for Different Cumulative Fractional Area Rock Coverage

Rock Diameter Interval (m)	Number of Rocks for Percentage CFA						
	1%	3%	5%	10%	20%	30%	40%
0.05–1.0	3.4	9.3	13.2	21.2	35.5	49.4	63.2
0.07–1.0	1.4	5.1	7.7	12.9	22.2	31.2	40.0
0.1–1.0	0.5	2.5	4.1	7.4	13.1	18.6	24.0
0.02–0.07	20.4	33.6	42.1	60.5	95.4	130.0	164.4
0.05–0.07	2.0	4.2	5.5	8.3	13.3	18.2	23.1
0.05–0.1	2.9	6.8	9.1	13.9	22.4	30.8	39.1

rocks seen from the landers are resolved by HiRISE. As a result, at all three rocky landing sites HiRISE is imaging the same population of rocks seen in lander images. Because the size-frequency distributions from HiRISE parallel the same exponential model curves based on lander rock distributions for the total rock coverage, the model distributions can be applied to larger diameters (and larger areas). These results indicate the size-frequency distributions at >1.5 m diameter can be extrapolated along model curves to estimate the number of rocks at diameters smaller than can be resolved by HiRISE.

[52] Maps of rock abundance of all HiRISE images in the Phoenix landing ellipse show areas with 0–1, 2–3, 4–8, 9–19, and >20 rocks per square hectare (10,000 m²) greater than 1.5 m in diameter. Size-frequency distributions of areas with these rock densities fall along model total rock coverages of ~5%, < 10%, < 15%, < 20%, and >21%. Extrapolation along the model distributions to the cumulative number of rocks larger than 0.7 m and 0.9 m diameter that exceed the lander leg clearance and 1.2 m diameter that could impede opening of the fan-shaped solar arrays allows the calculation of the probability of encountering one rock during these events. Because most of the valley selected for landing Phoenix is composed of low rock abundance surfaces (<10%), the probability the lander would encounter one rock higher than its base when landing or that might impede solar array deployment is <1%. These probabilities increase to ~3% and >5% for medium and high rock abundance surfaces.

[53] Extrapolation along the model distributions to the cumulative number of rocks 0.05–1 m diameter that would have ice free soil beneath them and 0.02–0.10 m diameter that could be picked up or pushed by the robotic arm allows calculation of the expected number of such rocks within reach after landing. Results suggest that even for low rock density areas, 20–60 pebbles small enough to be picked up by the robotic arm scoop are expected, and 3–20 rocks large enough to maintain ice free soil zones around them are within reach, of which 3–10 can be pushed by the arm. Rocks large enough to maintain ice free zones around them would likely reduce concerns that all soil would be dispersed by the descent engines during landing. Rocks that can be moved by the robotic arm would provide soil at greater depths for examining possible gradients in soil texture or chemistry with depth and possible gradients in thermal environment that could affect soil moisture and the presence of potential habitats and/or the deposition and accumulation of salts.

References

Arvidson, R. E., A. Carusi, A. Coradini, M. Fulchignoni, C. Federico, R. Funiciello, and M. Salmone (1976), Latitudinal variation of wind erosion of crater ejecta deposits on Mars, *Icarus*, 27, 503–516, doi:10.1016/0019-1035(76)90166-4.
Arvidson, R. E., E. Guinness, and S. Lee (1979), Differential aeolian redistribution rates on Mars, *Nature*, 278, 533–535, doi:10.1038/278533a0.
Arvidson, R. E., et al. (2008), Mars Exploration Program 2007 Phoenix landing site selection and characteristics, *J. Geophys. Res.*, 113, E00A03, doi:10.1029/2007JE003021.
Bonitz, R. G., et al. (2008), NASA Mars 2007 Phoenix lander robotic arm and icy soil acquisition device, *J. Geophys. Res.*, 113, E00A01, doi:10.1029/2007JE003030.
Bourke, R. (Ed.) (1989), Report of the mini-workshop on orbital imaging requirements for the Mars Rover Sample Return Mission, *JPL Tech. Rep. D-6442*, Jet Propul. Lab., Pasadena, Calif., 15 May.
Brown, W. K., and K. H. Wohletz (1995), Derivation of the Weibull distribution based on physical principles and its connection to the Rosin-Rammler and lognormal distributions, *J. Appl. Phys.*, 78, 2758–2763, doi:10.1063/1.360073.
Cheng, Y., A. Johnson, L. Matthies, and A. Wolf (2001), Passive imaging based hazard avoidance for spacecraft safe landing, paper presented at the 9th International Symposium on Artificial Intelligence, Robotics and Automation for Space (I-SAIRAS), Jet Propul. Lab., Montreal, Quebec, Canada, June.
Cheng, Y., A. Johnson, C. Olson, and L. Matthies (2003), Optical landmark detection for spacecraft navigation, paper presented at the 13th Annual American Astronautical Society (AAS/AIAA) Space Flight Mechanics Meeting, Ponce, Puerto Rico, Feb.
Christensen, P. R. (1986), The spatial distribution of rocks on Mars, *Icarus*, 68, 217–238, doi:10.1016/0019-1035(86)90020-5.
Christensen, P. R., and H. J. Moore (1992), The Martian surface layer, in *Mars*, edited by H. H. Kieffer et al., pp. 686–727, Univ. of Ariz. Press, Tucson.
Craddock, R. A., M. Golombek, and A. D. Howard (2000), Analyses of rock size-frequency distributions and morphometry of modified Hawaiian lava flows: Implications for future Martian landing sites, *Lunar Planet. Sci.*, XXXI, Abstract 1649.
Cramer, H. (1999), *Mathematical Methods of Statistics, Princeton Landmarks in Mathematics and Physics*, Princeton Univ. Press, Princeton, N. J.
Garvin, J. B., P. J. Mouginis-Mark, and J. W. Head (1981), Characterization of rock populations on planetary surfaces: Techniques and a preliminary analysis of Mars and Venus, *Moon Planets*, 24, 355–387, doi:10.1007/BF00897109.
Gilvarry, J. J. (1961), Fracture of brittle solids I. Distribution function for fragment size in single fracture (theoretical), *J. Appl. Phys.*, 32, 391–399, doi:10.1063/1.1736016.
Gilvarry, J. J., and B. H. Bergstrom (1961), Fracture of brittle solids II. Distribution function for fragment size in single fracture (experimental), *J. Appl. Phys.*, 32, 400–410, doi:10.1063/1.1736017.
Golombek, M., and D. Rapp (1997), Size-frequency distributions of rocks on Mars and Earth analog sites: Implications for future landed missions, *J. Geophys. Res.*, 102, 4117–4129, doi:10.1029/96JE03319.
Golombek, M. P., H. J. Moore, A. F. C. Haldemann, T. J. Parker, and J. T. Schofield (1999), Assessment of Mars Pathfinder landing site predictions, *J. Geophys. Res.*, 104, 8585–8594, doi:10.1029/1998JE900015.
Golombek, M. P., et al. (2003), Rock size-frequency distributions on Mars and implications for Mars Exploration Rover landing safety and operations, *J. Geophys. Res.*, 108(E12), 8086, doi:10.1029/2002JE002035.
Golombek, M. P., et al. (2005), Assessment of Mars Exploration Rover landing site predictions, *Nature*, 436, 44–48, doi:10.1038/nature03600.
Golombek, M. P., et al. (2006), Geology of the Gusev cratered plains from the Spirit rover transverse, *J. Geophys. Res.*, 111, E02S07, doi:10.1029/2005JE002503.
Golombek, M. P., R. E. Arvidson, T. Heet, L. Barry, J. R. Matijevic, and A. S. McEwen (2007), Size-frequency distributions of rocks on the northern plains of Mars in HiRISE Images with special reference to Phoenix landing sites, *Lunar Planet. Sci.*, XXXVIII, Abstract 1405.
Golombek, M. P., et al. (2008), Martian surface properties from joint analysis of orbital, Earth-based, and surface observations, in *The Martian Surface: Composition, Mineralogy and Physical Properties*, edited by J. Bell, pp. 468–497, Cambridge Univ. Press, New York.

Grant, J. A., S. A. Wilson, S. W. Ruff, M. P. Golombek, and D. L. Koestler (2006), Distribution of rocks on the Gusev Plains and on Husband Hill, Mars, *Geophys. Res. Lett.*, *33*, L16202, doi:10.1029/2006GL026964.

Greeley, R., R. O. Kuzmin, and R. M. Haberle (2001), Aeolian processes and their effects on understanding the chronology of Mars, *Space Sci. Rev.*, *96*, 393–404, doi:10.1023/A:1011917910624.

Haight, F. (1967), *Handbook of the Poisson Distribution, Publ. Oper. Res.*, vol. 11, 168 pp., John Wiley, New York.

Huertas, A., Y. Cheng, and R. Madison (2006), Passive imaging-based multi-cue hazard detection for spacecraft landing, paper presented at the 2006 IEEE Aerospace Conference, Big Sky, Mont., March.

Huertas, A., Y. Cheng, and L. Matthies (2007), Real-time hazard detection for landers, paper presented at the NASA Science Technology Conference, Adelphi, Md., May.

Kapur, J., P. Sahoo, and A. Wong (1985), A new method for gray-level picture thresholding using the entropy of the histogram, *Comput. Visual Graph. Image Processes*, *29*(3), 273–285, doi:10.1016/0734-189X(85)90125-2.

Kieffer, H. H., T. Z. Martin, A. R. Peterfreund, B. M. Jakosky, E. D. Miner, and F. D. Palluconi (1977), Thermal and albedo mapping of Mars during the Viking primary mission, *J. Geophys. Res.*, *82*, 4249–4291, doi:10.1029/JS082i028p04249.

Kirk, R. L., et al. (2008), Ultrahigh resolution topographic mapping of Mars with MRO HiRISE stereo images: Meter-scale slopes of candidate Phoenix landing sites, *J. Geophys. Res.*, doi:10.1029/2007JE003000, in press.

Malin, M. C., and K. S. Edgett (2001), Mars Global Surveyor Mars Orbiter Camera: Interplanetary cruise through primary mission, *J. Geophys. Res.*, *106*, 23,429–23,570, doi:10.1029/2000JE001455.

Marlow, J. J., C. R. Klein, M. M. Martinez, B. S. McGrane, and M. P. Golombek (2006), Boulder hazard assessment of potential Phoenix landing sites, *Lunar Planet. Sci.*, *XXXVII*, Abstract 1094.

Matthies, L., A. Huertas, Y. Cheng, and A. Johnson (2007), Landing hazard detection with stereo vision and shadow analysis, paper presented at the 17th Annual American Astronautical Society Infotech, Rohnert Park, Calif., May.

McCauley, J. F. (1973), Mariner 9 evidence for wind erosion in the equatorial and mid-latitude regions of Mars, *J. Geophys. Res.*, *78*, 4123–4137, doi:10.1029/JB078i020p04123.

McEwen, A. S., et al. (2007a), Mars Reconnaissance Orbiter's High Resolution Imaging Science Experiment (HiRISE), *J. Geophys. Res.*, *112*, E05S02, doi:10.1029/2005JE002605.

McEwen, A. S., et al. (2007b), A closer look at water-related geologic activity on Mars, *Science*, *317*(5845), 1706–1709, doi:10.1126/science.1143987.

McGrane, B. S., and M. P. Golombek (2006), Geomorphology context and THEMIS appearance of boulder fields in Phoenix landing region B, *Lunar Planet. Sci.*, *XXXVII*, Abstract 1541.

Mellon, M. T., W. V. Boynton, W. C. Feldman, J. L. Bandfield, T. N. Titus, D. A. Paige, A. Hock, N. E. Putzig, R. E. Arvidson, and H. G. Sizemore (2008), A prelanding assessment of the ice table depth and ground ice characteristics in Martian permafrost at the Phoenix landing site, *J. Geophys. Res.*, doi:10.1029/2007JE003067, in press.

Moore, H. J., and B. M. Jakosky (1989), Viking landing sites, remote-sensing observations, and physical properties of Martian surface materials, *Icarus*, *81*, 164–184, doi:10.1016/0019-1035(89)90132-2.

Moore, H. J., and J. M. Keller (1990), Surface-material maps of Viking landing sites on Mars, in *Reports of Planetary Geology and Geophysics Program—1989, NASA Tech. Memo., TM-4210*, 533–535.

Moore, H. J., and J. M. Keller (1991), Surface-material maps of Viking landing sites on Mars, in *Reports of Planetary Geology and Geophysics Program—1990, NASA Tech. Memo., TM-4300*, 160–162.

Moore, H. J., R. E. Hutton, G. D. Clow, and C. R. Spitzer (1987), Physical properties of the surface materials of the Viking landing sites on Mars, *U.S. Geol. Surv. Prof. Pap., 1389*, 222 pp., 2 plates.

Mutch, T. A., et al. (1977), The geology of the Viking Lander 2 site, *J. Geophys. Res.*, *82*, 4452–4467, doi:10.1029/JS082i028p04452.

Nowicki, S. A., and P. R. Christensen (2007), Rock abundance on Mars from the Thermal Emission Spectrometer, *J. Geophys. Res.*, *112*, E05007, doi:10.1029/2006JE002798.

Plemmons, D. H., et al. (2008), Effects of the Phoenix lander descent thruster plume on the Martian surface, *J. Geophys. Res.*, doi:10.1029/2007JE003059, in press.

Putzig, N. E., M. T. Mellon, M. P. Golombek, and R. E. Arvidson (2006), Thermophysical properties of the Phoenix Mars landing site study regions, *Lunar Planet. Sci.*, *XXXVII*, Abstract 2426.

Rosin, P., and E. Rammler (1933), The laws governing the fineness of powdered coal, *J. Inst. Fuel*, *7*, 29–36.

Seelos, K., et al. (2008), Geomorphologic and mineralogic characterization of the northern plains of Mars at the Phoenix Mission candidate landing sites, *J. Geophys. Res.*, doi:10.1029/2008JE003088, in press.

Sizemore, H. G., and M. T. Mellon (2006), Effects of soil heterogeneity on Martian ground-ice stability and orbital estimates of ice table depth, *Icarus*, *185*, 358–369, doi:10.1016/j.icarus.2006.07.018.

Smith, P. H., et al. (2008), The Phoenix mission to Mars, *J. Geophys. Res.*, doi:10.1029/2008JE003083, in press.

Wilhelms, D. E. (1987), The geologic history of the Moon, *U.S. Geol. Surv. Prof.*, 1348.

Wohletz, K. H., M. F. Sheridan, and W. K. Brown (1989), Particle size distributions and the sequential fragmentation/transport theory applied to volcanic ash, *J. Geophys. Res.*, *94*, 15,703–15,721, doi:10.1029/JB094iB11p15703.

Yingst, R. A., A. F. C. Haldemann, K. L. Biedermann, and A. M. Monhead (2007), Quantitative morphology of rocks at the Mars Pathfinder landing site, *J. Geophys. Res.*, *112*, E06002, doi:10.1029/2005JE002582.

————————

D. Adams, Y. Cheng, M. P. Golombek, A. Huertas, J. R. Matijevic, T. Parker, and L. K. Tamppari, Jet Propulsion Laboratory, California Institute of Technology, Pasadena, CA 91109, USA. (mgolombek@jpl.nasa. gov)

R. E. Arvidson, L. Barry, and T. Heet, Department of Earth and Planetary Sciences, Washington University at St. Louis, St. Louis, MO 63130, USA.

C. Klein, Department of Astronomy, California Institute of Technology, Pasadena, CA 91125, USA.

W. Li, Department of Computation and Neural Systems, California Institute of Technology, Pasadena, CA 91125, USA.

J. Marlow, Department of Earth Science and Engineering, Imperial College, London SW7 2AZ, UK.

M. Martinez, Department of Aeronautics and Astronautics, University of Washington, Seattle, WA 98195, USA.

A. S. McEwen, Lunar and Planetary Laboratory, University of Arizona, Tucson, AZ 85721, USA.

B. McGrane, Department of Geology, Occidental College, Los Angeles, CA 90041, USA.

M. Mellon and H. G. Sizemore, Laboratory for Atmospheric and Space Physics, University of Colorado, Boulder, CO 80309, USA.

K. Seelos, Applied Physics Laboratory, Johns Hopkins University, Laurel, MD 20723, USA.